Graphical Abstract

Synthesis

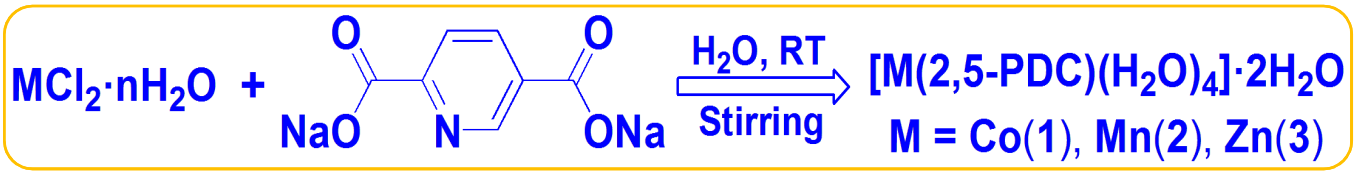

Molecular Structures

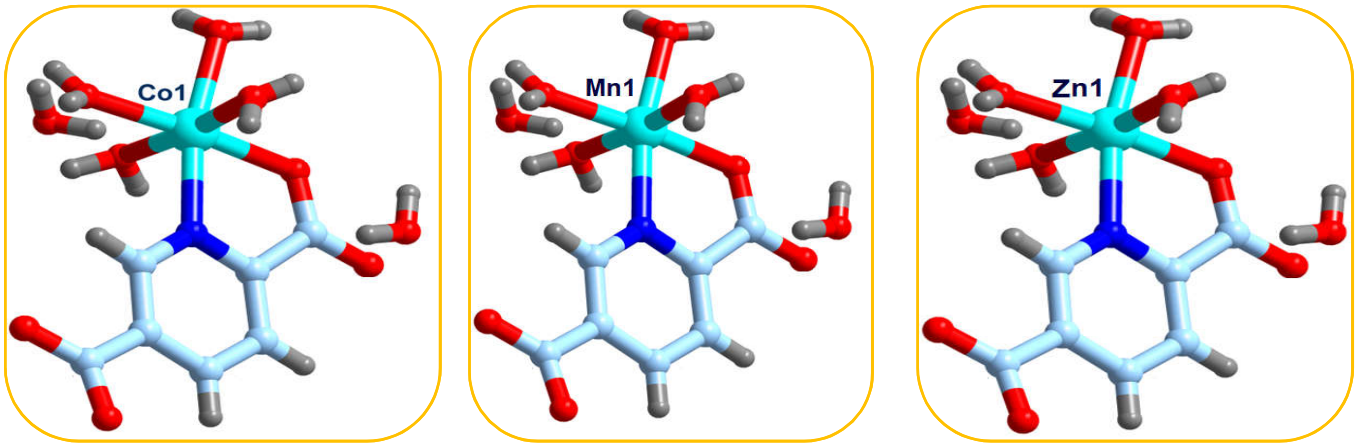

1 2 3

Self-Assembly

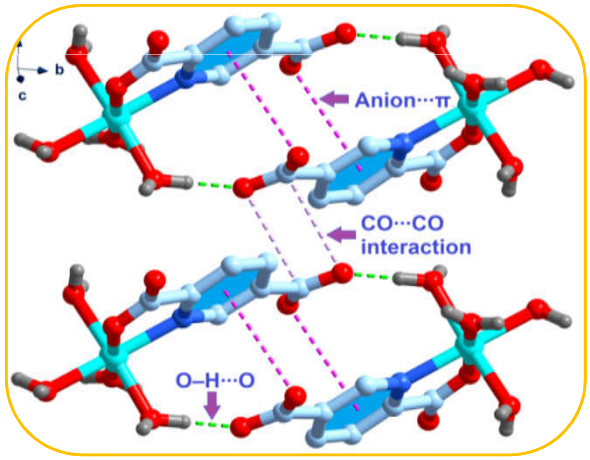

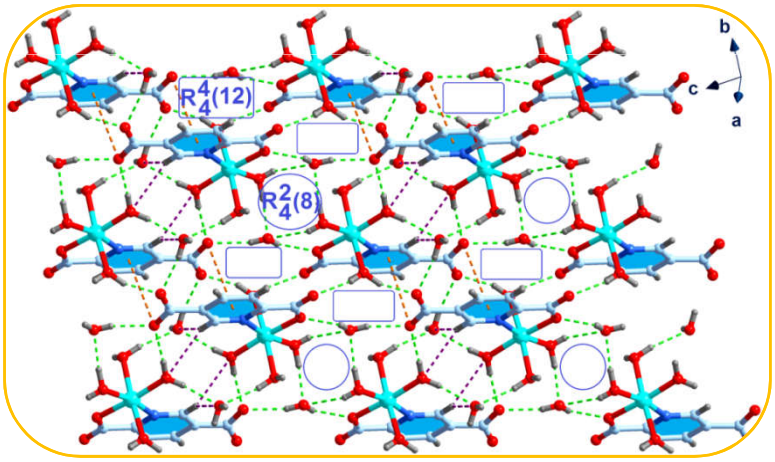

MTT & Apoptosis Assays

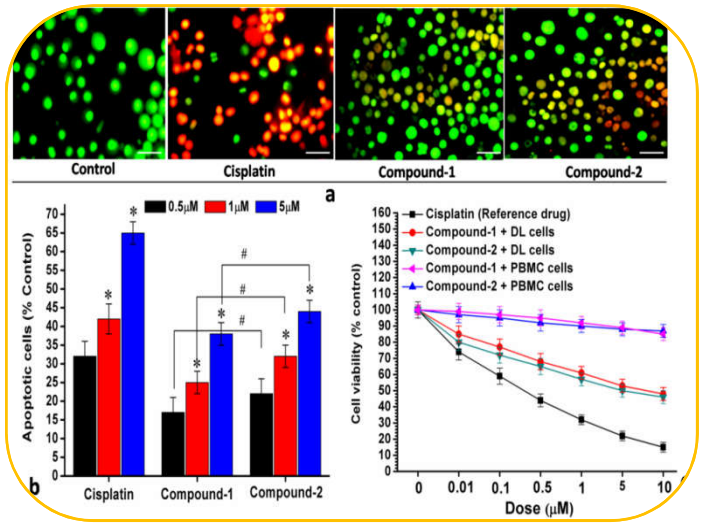

NCI Plot

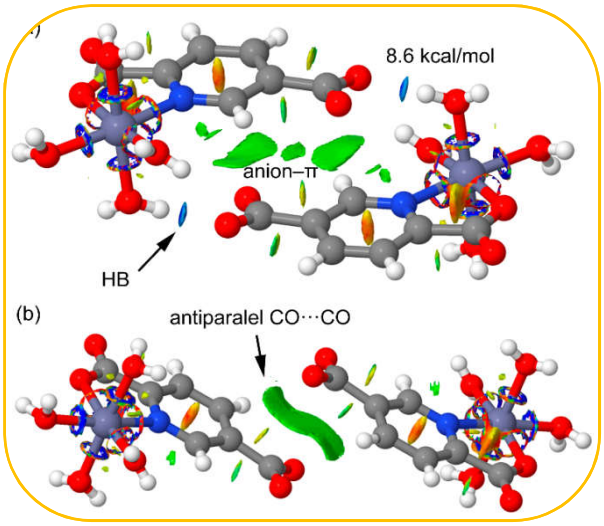

Chapter 2

Synthesis and Structural investigations of Isostructural Co(II), Mn(II) and Zn(II) Coordination Compounds involving 2,5-Pyridinedicarboxylate: Supramolecular Assemblies, Antiproliferative Evaluation and Theoretical Studies

2.1 INTRODUCTION

In recent years, crystal engineering of coordination complexes has received a great deal of interest not only due to their potential applications in catalysis, adsorption, magnetism, molecular recognition, nonlinear optics and sensors but also due to their intriguing structural architectures and topologies.[1] The structural diversity and the construction of such promising architectures strongly depend on the coordination geometries of the central metal ion and the chemical nature of the ligands.[2] Multifunctional pyridinedicarboxylic acid and its derivatives are often used to construct such network architectures with interesting topologies.[3]

K. K. Gangu *et al*. have recently reported a cobalt based metal organic framework of 2,5-pyridinedicarboxylate, *viz*. $[Co(2,5\text{-}PDC)(H_2O)_2]\cdot H_2O$ (where PDC = pyridinedicarboxylate) which exhibits catalytic activities in the synthesis of tetrahydrobiphenylene-1,3-dicarbonitrile derivatives.[4] The supramolecular architecture of the complex was stabilized by aromatic π–π and O–H···O hydrogen bonding interactions. The carboxylate-based coordination compounds are important in the fields of supramolecular chemistry and crystal engineering for their rich biochemistry, since they exhibit numerous biological activities such as antitumor, anti-candida and anti-microbial etc.[5]

Pyridine 2,5-dicarboxylic acid serves as a suitable H-bonding acceptor[6] and can give rise to the formation of bridging coordination compounds with potential variety in self-assembly processes.[7] Recent studies have revealed its rich solid-state coordination modes in inorganic-organic mixed ligand complexes involving transition and rare-earth metals.[8] B. Ey *et al.* have recently reported the photoluminescence properties and heterogeneous catalytic activities of two isostructural coordination complexes involving *2,5-PDC*.[9] In addition, many groups have recently reported the anticancer activities of various transition metal compounds of pyridinedicarboxylates.[10]

Non-covalent interactions in coordination compounds form the backbone of supramolecular assemblies that include hydrogen bond, stacking, electrostatic and charge-transfer interactions as well as metal ion coordination.[11] Supramolecular interactions involving aromatic systems, *viz*. the anion-π[12] and lone pair (lp)-π[13] interactions also contribute towards stability of such structures. Anion-π interaction, broadly defined as an attraction of anions to electron-deficient π-systems[14], plays important roles in various biological systems.[15] Electrostatic charge-quadruple moment and correlation interactions play crucial roles in such non-covalent interactions involving aromatic π-electron systems; however, experimental and computational studies on the intrinsic anion-π interactions are scarce in the literature.[16] Egli and co-workers have extended this concept to a more general form, namely, lone pair (l.p)-π interactions. Very recently, in a comprehensive review[17], Gamez *et al.* designated such lone pair (l.p)-π contacts as a new supramolecular interaction and rigorous analysis of the Cambridge Structure Database (CSD) revealed that such contacts are not unusual in the structures of inorganic/coordination compounds but have been overlooked in the past.[18]

Carbonyl groups are ubiquitous in organic and biological systems and their molecular recognition properties have been studied extensively.[19] It has been observed that the columbic interactions between the C and O atoms of proximal -CONH groups in proteins are one of the important factors for the stability of α-helices, β-sheets and for the right-hand twist, often observed in β-strands.[20] The dipolar interaction between carbonyl groups in stabilizing the packing modes of small organic molecules is comparable to that of the medium strength hydrogen bonds as well as other non-

covalent interactions observed in supramolecular recognition processes.[21] Three common CO···CO interaction motifs are observed in crystal structures (**Scheme 2.1**): (a) a highly sheared parallel motif (S), (b) a perpendicular motif (P) and (c) a slightly sheared antiparallel motif involving a pair of short C···O interactions (A).[21]

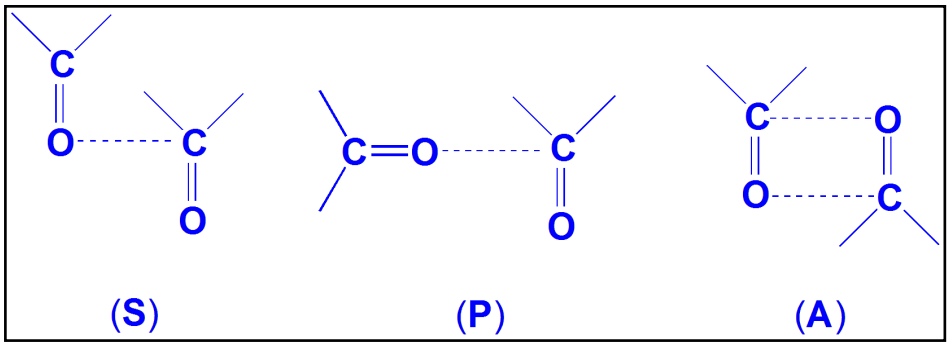

Scheme 2.1 Schematic representations of the three motifs for CO···CO interactions.

In order to further explore the presence of such anion-π and unconventional anti-parallel CO···CO interactions in 2,5-pyrindinedicarboxylate complexes, we, in this chapter, have reported three isostructural M(II) complexes (M = Co, Mn and Zn) of the type $[Co(2,5\text{-}PDC)(H_2O)_4]\cdot 2H_2O$ (**1**), $[Mn(2,5\text{-}PDC)(H_2O)_4]\cdot 2H_2O$ (**2**) and $[Zn(2,5\text{-}PDC)(H_2O)_4]\cdot 2H_2O$ (**3**). We also aim to evaluate the isostructurality parameters of the compounds **1**, **2** and **3** using Fabian and Kalman approach. Apart from discussing their syntheses and crystal structures, the unconventional anti-parallel CO···CO and anion-π interactions are analyzed theoretically by using DFT calculations, MEP surfaces and NCI plot. The anticancer potential of complexes **1** and **2** were validated *in vitro* in Dalton's Lymphoma (DL) malignant cancer cell line considering cytotoxicity, apoptosis and molecular docking as parameters. Anti-apoptotic BCL family proteins, *viz*. BCL-2, BCL-XL and MCL-1 were docked with complexes **1** and **2** to dissect possible molecular mode of action associated with apoptosis in DL malignant cancer cell line.

2.2 EXPERIMENTAL

2.2.1 Materials and methods

All reagents used in this work were obtained from Sigma Aldrich and Merck (India) Ltd. and used without further purification. De-ionized water was used as the

reaction medium. Elemental (C, H and N) analyses were carried out using Perkin Elmer 2400 Series II CHNS/O analyzer. KBr phase FT-IR spectra were recorded in Brukar APEX II FTIR spectrophotometer in the mid-IR region (4000 to 500 cm^{-1}). The diffuse-reflectance UV-Vis-NIR spectra were recorded using Shimadzu UV-2600 spectrophotometer. Thermogravimetric studies were carried out under the flow of N_2 gas using Mettler Toledo TGA/DSC1 STAR^e system at the heating rate of $10^oC\ min^{-1}$. The powder X-ray diffraction (PXRD) data were recorded using XPERT-PRO X-ray powder diffractometer with Cu-Kα radiation. Room temperature magnetic susceptibility was measured at 300 K on a Sherwood Mark 1 Magnetic Susceptibility balance by Evans method.

2.2.2 Preparation of the complexes

2.2.2.1 Preparation of [Co(2,5-PDC)$(H_2O)_4$]·$2H_2O$ (1)

Cobalt(II) chloride hexahydrate, $CoCl_2{\cdot}6H_2O$ (0.238 g, 1 mmol) and disodium 2,5-pyridinedicarboxylate (0.211 g, 1 mmol) were dissolved in 10 mL de-ionised water in a round bottom flask. The solution was stirred at room temperature for about an hour. The red precipitate so obtained was then filtered and the filtrate was left unperturbed in cooling conditions for crystallization. After a few weeks, block shaped, reddish single crystals of **1** suitable for X-ray analysis were obtained with 86% yield (0.287 g) (**Scheme 2.2**). The large crystals were filtered off, washed with excess water and dried in air. Anal. calcd. for $C_7H_{15}CoNO_{10}$ (Mw = 332.13): C, 25.31%; H, 4.55%; N, 4.22%. Found: C, 25.25%; H, 4.47%; N, 4.19%; IR spectral data (KBr disc, cm^{-1}): 3279(br), 1663(s), 1398(s), 1266(s), 1179(w), 1039(m), 840(s), 686(sh), 583(w) [s, strong; m, medium; w, weak; br, broad; sh, shoulder]. μ_{eff} = 3.87 BM.

2.2.2.2 Preparation of [Mn(2,5-PDC)$(H_2O)_4$]·$2H_2O$ (2)

A similar procedure as that for **1** was employed for the synthesis of **2** with the exception that in place of cobalt(II) chloride hexahydrate, $CoCl_2{\cdot}6H_2O$, manganese(II) chloride tetrahydrate, $MnCl_2{\cdot}4H_2O$ (0.198 g, 1 mmol) was used (**Scheme 2.2**). The colourless product so obtained was then filtered and the filtrate was left unperturbed in cooling conditions for crystallization. Colourless block shaped single crystals of **2**

suitable for X-ray analysis was obtained with 89% yield (0.294 g). Anal. calcd. for $C_7H_{15}MnNO_{10}$ (Mw = 328.14): C, 25.62%; H, 4.61%; N, 4.27%. Found: C, 25.54%; H, 4.55%; N, 4.18%; IR spectral data (KBr disc, cm^{-1}): 3373(br), 1633(s), 1478(m), 1398(s), 1281(s), 1179(s), 1120(s), 1031(s), 832(m), 759(s), 694(m), 532(w) [s, strong; m, medium; w, weak; br, broad; sh, shoulder]. μ_{eff} = 5.92 BM.

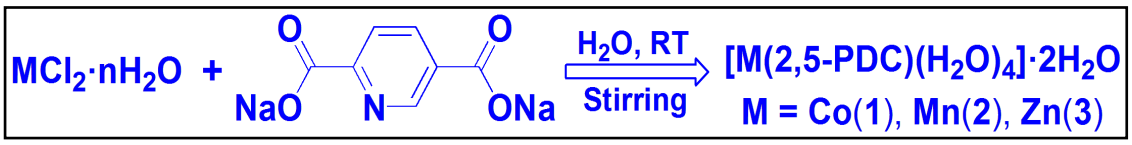

Scheme 2.2 Synthesis of compounds **1**, **2** and **3**.

2.2.2.3 Preparation of [Zn(2,5-PDC)$(H_2O)_4$]·$2H_2O$ (3)

Compound **3** was prepared by using the similar procedure, except that zinc(II) chloride, $ZnCl_2$ (0.136 g, 1mmol) was used as the metal salt (**Scheme 2.2**). Colourless product so obtained was then filtered and the filtrate was left unperturbed in cooling conditions for crystallization. Colourless and needle shaped single crystals of **3** suitable for X-ray analysis were obtained with 86% yield (0.291 g). Anal. calcd. for $C_7H_{15}ZnNO_{10}$ (Mw = 338.57): C, 24.83%; H, 4.47%; N, 4.14%. Found: C, 24.72%; H, 4.41%; N, 4.03%; IR spectral data (KBr disc, cm^{-1}): 3388(br), 1653(s), 1476(m), 1395(s), 1366(s), 1285(s), 1176(s), 1036(s), 888(m), 754(s), 691(m), 539(w) [s, strong; m, medium; w, weak; br, broad; sh, shoulder].

2.2.3 X-ray crystallographic procedures

Molecular and crystal structures of **1**, **2** and **3** were determined by single crystal X-ray diffraction technique. X-ray diffraction data collection was carried out on a Bruker SMART CCD diffractometer with graphite mono-chromatized Mo Kα radiation (λ = 0.71073 Å). Semi-empirical absorption correction, as well as scaling and merging the different datasets for each wavelength were performed with SADABS.[22] Crystal structures were solved by direct method (SHELXS) and refined by full matrix least squares techniques (SHELXL-2018/3) using the WinGX[23] platform available for the

personal computers. All the non-hydrogen atoms were refined anisotropically. The hydrogen atoms in both the complexes, except those attached to oxygen atoms of water molecules were located in difference Fourier maps and refined with isotropic atomic displacement parameters. The hydrogen atoms of the lattice water molecules could not be located from the difference Fourier maps and are fixed at their normalized distances to obtain the hydrogen bonding patterns in the crystal structure. The crystal of compound **2** was moderately diffracting, so few poor reflections were deleted during integration. This resulted in low data completeness. The structural diagrams were drawn with Diamond 3.2.[24] Data collection refinement parameters for the complexes **1**, **2** and **3** are summarized in **Table 2.1**.

2.2.4 Theoretical methods

The geometries of the complexes included in this study were computed at the M06-2X/def2-TZVP level of theory using the crystallographic coordinates. For the calculations we have used the GAUSSIAN-09 program.[25] We have also used the Grimme's dispersion[26] correction since it is adequate for the evaluation of non-covalent interactions. The basis set superposition error for the calculation of interaction energies has been corrected using the counterpoise method.[27] The NCI plot[28] iso-surfaces have been used to characterize non-covalent interactions. They correspond to both favorable and unfavorable interactions, as differentiated by the sign of the second density Hessian Eigen value and defined by the iso-surface colour. The colour scheme is a red-yellow-green-blue scale with red for ρ^{+}_{cut} (repulsive) and blue for ρ^{-}_{cut} (attractive). The Gaussian-09 B3LYP-D/6-31+G* level of theory wave function has been used to generate the NCI plot.

2.2.5 Cell line and drug preparation

The anticancer activities of compounds **1** and **2** were carried out in *in vitro* condition for 24 hours using Dalton's lymphoma (DL) cell line. The DL cells were cultured in RPMI-1640 supplemented with 10% FBS, gentamycin (20 mg/mL), streptomycin (100 mg/mL) and penicillin (100 IU) in a CO_2 incubator at 37°C with 5% CO_2; 80% confluent of exponentially growing cells were sub-cultured and used in the

2.2.6 Crystal data

Table 2.1 Crystal and structure refinement data for **1**, **2** and **3**.

Parameters	**1** (Co)	**2** (Mn)	**3** (Zn)
Emprical formula	$C_7H_{15}CoNO_{10}$	$C_7H_{15}MnNO_{10}$	$C_7H_{15}NO_{10}Zn$
Formulae weight	332.13	328.14	338.57
Temperature (K)	293(2)	293(2)	293(2)
Wavelength (Å)	0.71073	0.71073	0.71073
Crystal system, space group	Triclinic, $P\bar{1}$	Triclinic, $P\bar{1}$	Triclinic, $P\bar{1}$
a/Å	7.0788(2)	7.0957(4)	7.1007(3)
b/Å	8.3640(2)	8.3505(5)	8.3500(4)
c/Å	11.4416(4)	11.4684(9)	11.4727(7)
α^o	107.115(2)	107.130(5)	107.050(3)
β^o	99.326(2)	99.493(4)	99.449(3)
γ^o	102.718(10)	102.789(3)	102.753(2)
Volume ($Å^3$)	612.56(3)	613.67(7)	614.88(5)
Z, Calculated density (Mgm^{-3})	2, 1.801	2, 1.776	2, 1.829
Absorption coefficient (mm^{-1})	1.451	1.126	2.047
F(000)	342	338	348
Crystal size (mm^3)	0.28×0.20×0.15	0.32×0.25×0.17	0.35×0.26×0.16
θ range for data collection (^{o})	1.92 to 25.00	1.92 to 25.23	1.92 to 27.30
Index ranges	-8<=h<=8, -9<=k<=9,-13<=l<=13	-8<=h<=8,-10<=k<=10,-12<=l<=13	-8<=h<=9, -10<=k<=10,-13<=l<=13
Reflections collected	8317/2109 [*R*(int) =0.0187]	6852/2047 [*R*(int) =0.0213]	6991/2147[*R*(int) =0.0197]
Refinement method	Full-matrix least-squares on F^2	Full-matrix least-squares on F^2	Full-matrix least-squares on F^2
Data / restraints / parameters	2109/0/208	2047/20/174	2147/0/175
Goodness-of-fit on F^2	1.097	1.090	1.098
Final *R* indices[$I>2\sigma(I)$] *R*1/ *wR*2	0.0229/0.0605	0.0472/0.1411	0.0258/ 0.0684
R indices (all data) *R*1/ *wR*2	0.0243/0.0624	0.0521/0.1455	0.0300/0.0701
Largest diff. peak and hole	0.260 and -0.415	0.789 and -0.742	0.532 and -0.347

$wR2 = \{\Sigma [w(F_o^2 - F_c^2)^2] / \Sigma [w(F_o^2)^2] \}^{1/2}$; $R1 = \Sigma | |F_o| - |F_c| | / \Sigma |F_o|$ *GooF = $S = \{\Sigma [w(F_o^2 - F_c^2)^2] / (n-p)^2$

experiments. The different doses of compounds were prepared freshly during the experiments by dissolving in phosphate-buffered saline (pH = 7.4).

2.2.7 MTT Cell viability assay and IC_{50} measurement

The growth inhibitory effect of compounds **1** and **2** towards cancer cells were evaluated by means of MTT assay.[29] Briefly, $1x10^6$ cells/well, dependent upon the growth characteristics of the cell line, were seeded in 24-well micro plates in suitable growth medium (200 µL). After 24 hours, the medium was replaced with fresh media containing the compounds at the different concentrations (0, 0.01, 0.1, 0.5, 1, 5 and 10 µM). For each treatment, triplicate cultures were setup and after 24 hours, each well was treated with 10 µL of MTT (5 mg/mL) solution and following 3 hours of incubation, 100 µL of DMSO was added into each well. The plates were checked for complete solubilization of the purple formazan crystals under the inverted phase microscope and the mean absorbance for each compound was expressed as a percentage comparing with that of the untreated control group and plotted vs drug concentration. IC_{50} values, the drug concentrations that reduce the mean absorbance at 570 nm to 50% of those in the untreated control wells, were calculated by four parameter logistic (4-PL) model.[30]

2.2.8 Cell proliferation and apoptosis assay

Fluorescence based apoptotic cell death was determined using acridine orange and ethidium bromide (AO/EB) staining method.[31] AO is taken up by both viable and nonviable cells due to membrane permeability and emits green fluorescence if intercalated into double stranded nucleic acid (DNA), whereas; EB is taken up only by nonviable cells due to compromised membrane structure and emits red fluorescence after intercalation into DNA. Briefly, control and treated DL cells were collected after 24 hours of treatment with the compounds **1** and **2**, washed with phosphate-buffered saline (PBS) and to the cell suspension; AO/EB (100 µg/mL of each dye) was added, mixed gently and incubated for 5 min under dark chamber. Then cells were thoroughly examined under fluorescence microscope and photographed. About 1000 cells were analyzed, and the percentage of apoptotic nuclei was determined.

2.2.9 Molecular docking

The possible molecular interactions between compounds **1** and **2** and anti-apoptotic target proteins were predicted by Molegro Virtual Docker (MVD 2010.4.0) software for Windows.[32] The 3D coordinates of target proteins such as BCL-2 (PDB ID: 2O22), BCL-XL (PDB ID: 2YXJ), and MCL-1 (PDB ID: 5vkc) were retrieved from Protein Data Bank (PDB). Further, missing hydrogen atoms were added and bond orders were assigned to all target proteins. All the target proteins included in the present study were selected based on the potential roles in multiple cancer types. The molecular arrangement and geometry of both compounds were fully optimized using the semi-empirical quantum chemistry method (Parametric Method 3). The docking parameters were run using a GRID of 15 Å in radius and 0.30 in resolution with number of runs: 10 runs; algorithm: Moldock SE; maximum interactions: 1500; maximum population size: 50; maximum steps: 300; neighbor distance factor: 1.00; maximum number of poses returned: 5 to cover the ligand-biding site of the protein structures. Protein-ligand binding site was further analyzed and visualized by using Chimera software.[33]

2.2.10 Pharmacophore modelling

In modern computational and medicinal chemistry, pharmacophore features are used to identify the essential components of one or multiple molecules with the similar biological activities.[34] Pharmacophore features can be used to search for more molecules which share the same features when arranged in the same 3D orientations. In the present study, pharmacophore models of the compounds **1** and **2** were generated using Ligandscout software which demonstrated Structure Activity Relationship (SAR).[34] After performing molecular docking simulation, the obtained best docking orientation (pose) were loaded into Ligandscout software and key pharmacophore features were identified including H-bond donor, H-bond acceptor, hydrophobic, aromatic, positively and negatively ionizable groups.[35]

2.2.11 Statistical analysis

Experimental results are expressed as mean ± S.D. All measurements were replicated three times. The data were analyzed by an analysis of variance (ANOVA) ($P \leq 0.05$).[36] The IC_{50} values were calculated from linear regression analysis.[37]

2.3 RESULTS AND DISCUSSION

2.3.1 Synthesis and general aspects

The complexes $[Co(2,5\text{-PDC})(H_2O)_4]\cdot 2H_2O$ (**1**), $[Mn(2,5\text{-PDC})(H_2O)_4]\cdot 2H_2O$ (**2**) and $[Zn(2,5\text{-PDC})(H_2O)_4]\cdot 2H_2O$ (**3**) have been isolated in high yield by reacting one equivalent of respective metal chlorides (Co, Mn, Zn) with one equivalent of disodium 2,5-pyridinedicarboxylate in water. They are soluble in water; however, their solubility in common organic solvents is low. Interestingly, the products obtained for the compounds during the reaction resemble the single crystals obtained from the slow evaporation of the respective mother liquors which has been confirmed by the FT-IR spectral studies. Compounds **1** and **2** show room temperature μ_{eff} values of 3.87 and 5.92 BM respectively and confirm the high spin states of the respective metal ions.[38]

2.3.2 Spectral properties

2.3.2.1 FT-IR Spectroscopy

FT-IR spectra of the compounds **1**, **2** and **3** (KBr pellets) were recorded in the region 4000-500 cm^{-1} (**Figure 2.1**). The bands have been tentatively assigned on the basis of earlier reports in the literature.[39] Most of the IR band positions are similar due to the isostructural coordination environment around the metal ions in them. The strong and broad bands at around 3314, 3395 and 3388 cm^{-1} are assigned to the symmetric and anti-symmetric ν(O–H) stretching vibrations of lattice and/or coordinated water molecules of **1**, **2** and **3** respectively.[40] The absence of band at 1730 cm^{-1} in **1**, **2** and **3** indicates that *2,5-PDC* gets completely deprotonated upon coordination with the metal ions.[41] The difference between the asymmetric and symmetric carboxylate stretching [$\Delta\nu = \nu_{as}(COO^-) - \nu_s(COO^-)$] is often used for the correlation of the infrared spectra with the structures of metal carboxylates.[42] These values are approximately 228 cm^{-1} for monodentate, 164 cm^{-1} for ionic and 142 cm^{-1} for bidentate carboxylate groups.[43] The strong and sharp bands at 1658, 1638 and 1653 cm^{-1} are due to the asymmetric stretching vibrations, $\nu_{as}(COO^-)$ of carboxylate moiety of **1**, **2** and **3** respectively while the symmetric stretching vibration bands for them, $\nu_s(COO^-)$ appear at around 1409, 1397 and 1395 cm^{-1} respectively; the differences [$\Delta\nu = \nu_{as}(COO^-) - \nu_s(COO^-)$ = 249, 241 and 238 cm^{-1} respectively for **1**, **2** and **3**] indicate the monodentate behavior of the carboxylate moiety of *2,5-PDC* to the metal centers in all of them.[44] Similar Δν values

have been recently reported by N. Hojnik and his coworkers for the monodentate coordination of *2,6-PDC* to the metal centers.[45]

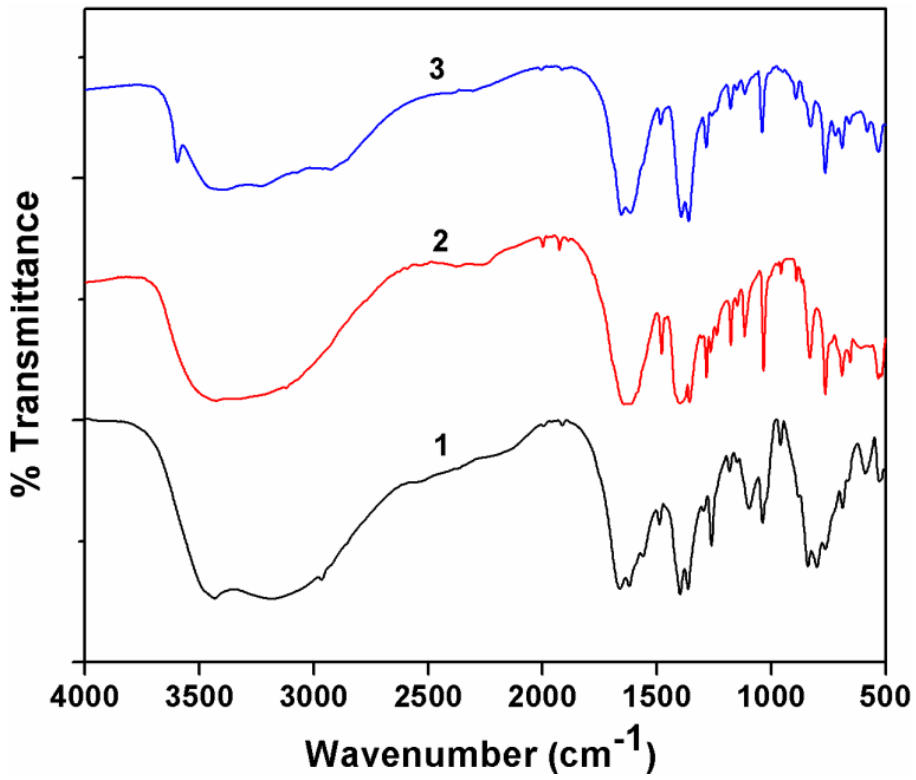

Figure 2.1 FT-IR spectra of compounds **1**, **2** and **3**.

2.3.2.2 Electronic Spectroscopy

Solid state UV-Vis-NIR spectrum of **1** exhibits intense peak at around 368 nm assigned to n→π* transitions of the aromatic ligand [**Figure 2.2**(**a**)]. We can expect three ligand field bands for the high-spin octahedral Co(II) complex *viz.* $^4T_{1g}(F)\rightarrow{}^4T_{2g}(F)$ (ν_1), $^4T_{1g}(F)\rightarrow{}^4A_{2g}(F)$ (ν_2) and $^4T_{1g}(F)\rightarrow{}^4T_{1g}(P)$ (ν_3). The first band occurs at 1024 nm, the third band is seen at 488 nm whereas the ν_2 band due to $^4T_{1g}(F)\rightarrow{}^4A_{2g}(F)$ appears at 538 nm.[46] However, the spectrum in water [**Figure 2.2**(**b**)] shows weak absorption bands at 467 and 513 nm assigned to $^4T_{1g}(F)\rightarrow{}^4T_{1g}(P)$ (ν_3) and $^4T_{1g}(F)\rightarrow{}^4A_{2g}(F)$ (ν_2) transitions. D. Dogan *et al.* have reported similar observation for the complex $[Co(en)_3][Co(2,5\text{-}PDC)_2(H_2O)_2]\cdot 2H_2O$; where 2,5-PDC = pyridine-2,5-dicarboxylate.[47] The NIR band is not seen in the solution spectrum because of the limit in the wavelength window of the spectrophotometer used.[37]

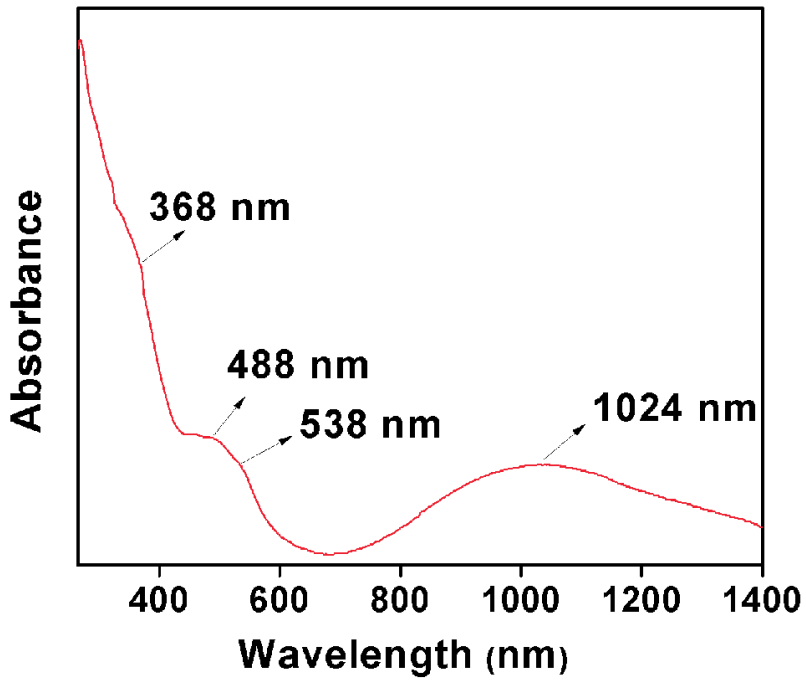

(**a**)

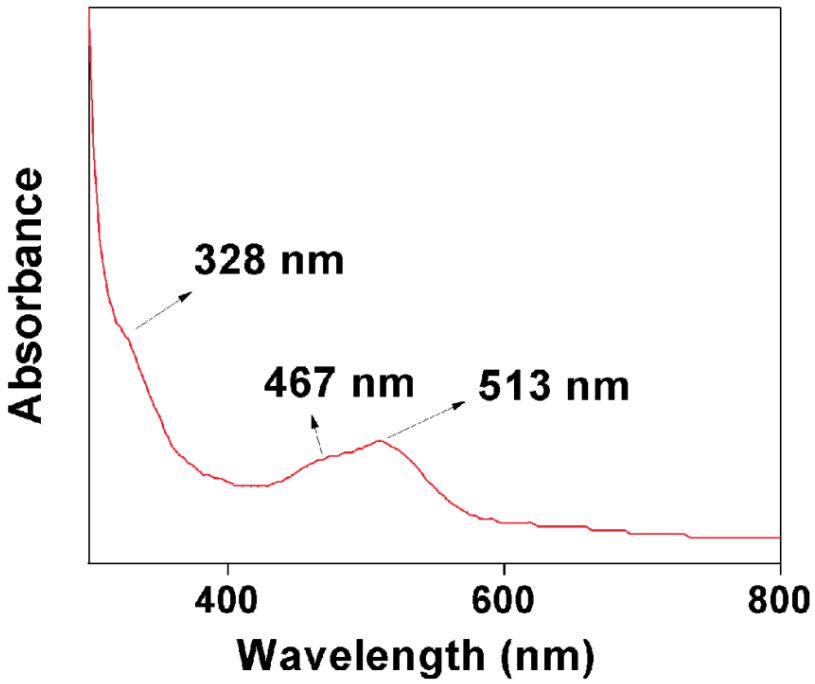

(**b**)

Figure 2.2 (**a**) UV-Vis-NIR spectrum of $[Co(2,5\text{-}PDC)(H_2O)_4]\cdot 2H_2O$ (**1**); (**b**) UV-Vis spectrum of $[Co(2,5\text{-}PDC)(H_2O)_4]\cdot 2H_2O$ (**1**) in water.

The UV-Visible spectra of **2** and **3** in aqueous phase are shown in **Figure 2.3** and **Figure 2.4** respectively. There are no d-d bands, because all electronic transitions from their ground state are doubly forbidden. The absorptions at 223 and 215 nm can be assigned to the intraligand $\pi \rightarrow \pi^*$ absorption of *2,5-PDC* ligand in **2** and **3** respectively. The bands at 271 and 263 nm are attributed to the LMCT (ligand to metal charge transfer) transitions.[48] In the solid state UV-Vis-NIR spectrum, however, these absorption peaks are obtained at 228, 265 nm and 275, 299 nm respectively.[49] The position of the absorption peaks in the solid and in aqueous phases for **1** and **2** do not show marked differences. Therefore, it may be assumed that bonding modes as well as the geometries of **1** and **2** do not change in the solution phase.[50]

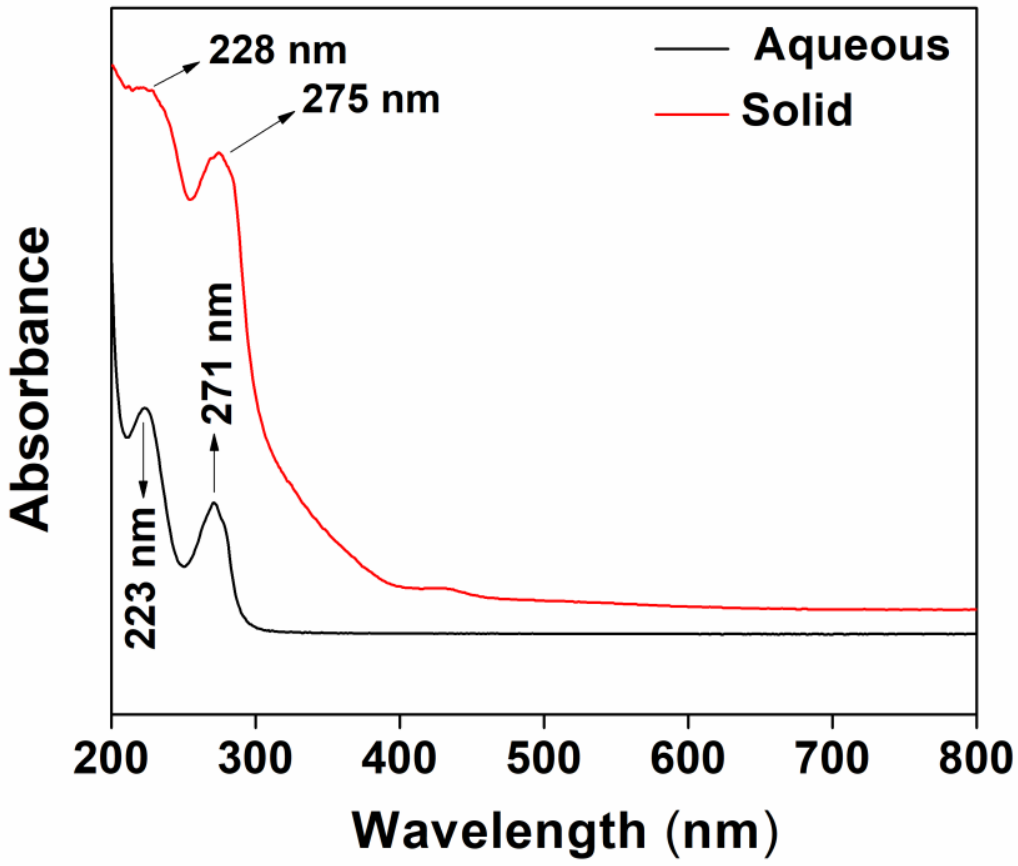

Figure 2.3 Electronic spectra of $[Mn(2,5\text{-}PDC)(H_2O)_4]\cdot 2H_2O$ (**2**) in solid and aqueous phases.

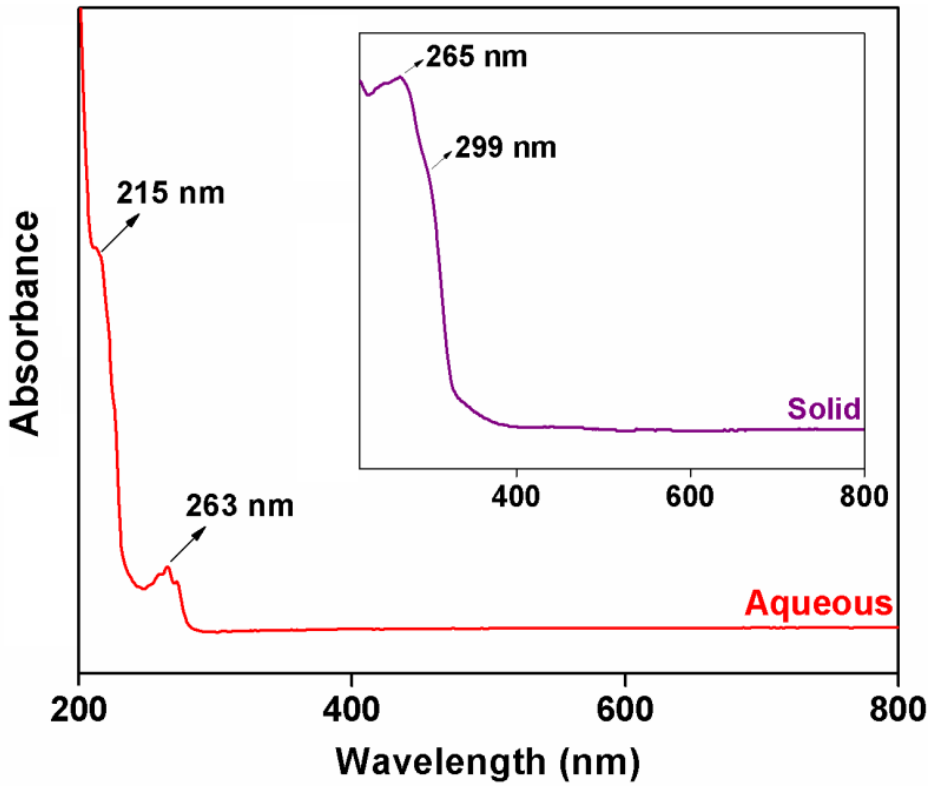

Figure 2.4 Electronic spectra of $[Zn(2,5\text{-PDC})(H_2O)_4]\cdot 2H_2O$ (**3**) in solid and aqueous phases.

2.3.3 Crystal structures

Single-crystal X-ray diffraction studies revealed that the complexes **1** (**Figure 2.5**), **2** (**Figure 2.6**) and **3** (**Figure 2.7**) are isostructural. They crystallize in the same triclinic space group ($P\bar{1}$) with similar unit cell parameters (**Table 2.1**). Their selected bond lengths (Å) and bond angles (°) are presented in **Table 2.2**. The three complexes being isostructural, the structure of **1** is described as a representative example in detail here. As shown in **Figure 2.5**, the metal center of **1** is surrounded by one doubly deprotonated bidentate chelating *2,5-PDC*, four coordinated and two lattice water molecules. The crystallographically unique metal center involving Co(II) in it is six-coordinated with one nitrogen and five oxygen atoms from one *2,5-PDC* anion and four coordinated water, resulting in a distorted octahedral coordination sphere (**Figure 2.5**). The equatorial plane of **1** is defined by O7 and O8 from two of the coordinated aqua ligands and O1 and N1 from *2,5-PDC* ligand. O6 and O5 from other coordinated water

molecules are positioned at the axial sites with the bond angle of 173.99(1)°. The sum of the bond angles (**Table 2.2**) of O1–Co1–N1, O8–Co1–N1, O7–Co1–O1 and O8–Co1–O7 in **1** is 360.269°, which suggests N1, O1, O7, and O8 atoms are almost co-planar (mean r.m.s. deviation of 0.0689 Å, 0.0584 Å and 0.0714 Å in **1**, **2** and **3** respectively). A comparative study shows that the average Co1–O1 distances are consistent with, but the Co1–N1 distances are a bit shorter, than the similar bond distances of previously reported Co(II) complexes of *2,5-PDC*.[51,52]

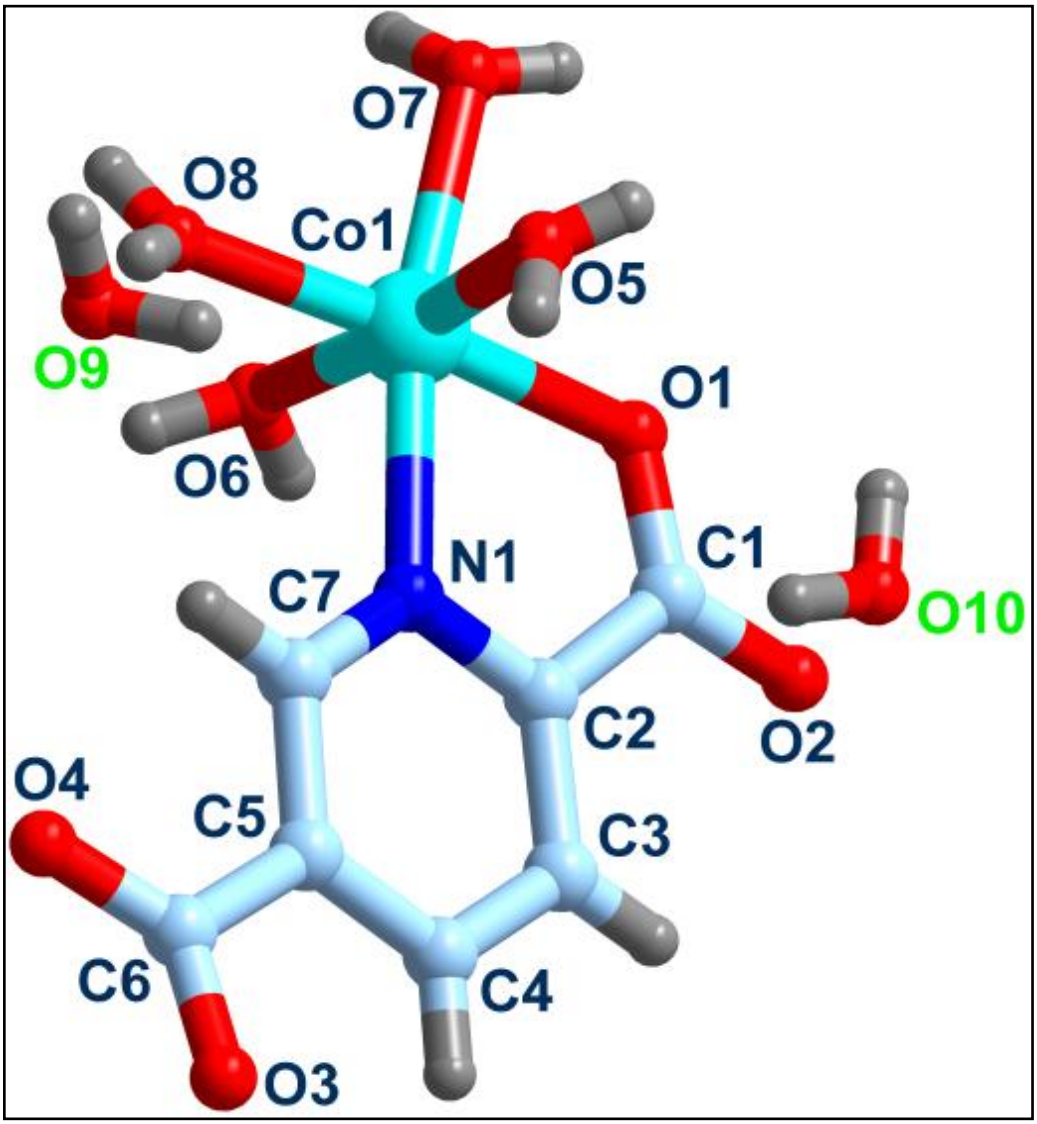

Figure 2.5 Molecular structure of $[Co(2,5\text{-}PDC)(H_2O)_4]\cdot 2H_2O$ (**1**).

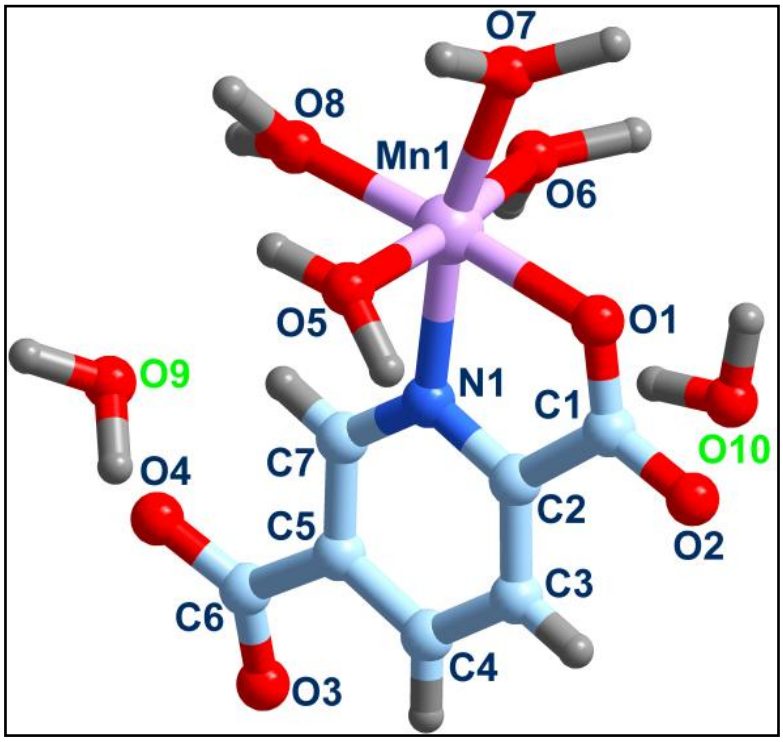

Figure 2.6 Molecular structure of [Mn(2,5-PDC)(H_2O)$_4$]·2H_2O (**2**).

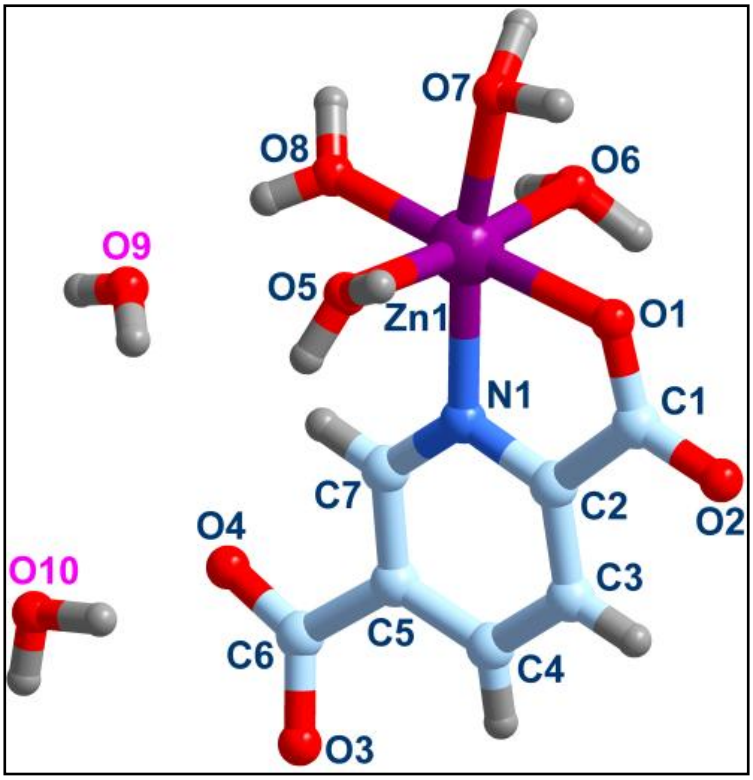

Figure 2.7 Molecular structure of [Zn(2,5-PDC)(H_2O)$_4$]·2H_2O (**3**).

Table 2.2 Selected bond lengths (Å) and angles (°) in metal core in **1**, **2** and **3**.

Bond lengths	**1**	**2**	**3**	Bond angles	**1**	**2**	**3**
M1–O1	2.068(1)	2.086(2)	2.095(1)	O1–M1–O6	88.94(6)	96.75(2)	88.96(6)
M1–O5	2.116(2)	2.173(1)	2.141(2)	O1–M1–O7	90.65(6)	88.96(3)	89.35(7)
M1–O6	2.151(2)	2.142(1)	2.170(2)	O1–M1–O8	174.01(2)	174.90(3)	174.04(7)
M1–O7	2.122(1)	2.110(2)	2.100(2)	O1–M1–O5	96.82(6)	89.06(2)	94.96(6)
M1–O8	2.047(2)	2.019(2)	2.044(2)	O1–M1–N1	78.13(6)	78.24(2)	78.12(7)
M1–N1	1.133(1)	1.130(1)	1.132(2)	O6–M1–O7	90.95(6)	86.58(3)	91.77(8)
				O6–M1–O8	85.33(6)	88.32(3)	85.29(8)
				O6–M1–O5	173.96(6)	173.97(3)	173.87(7)
				O6–M1–N1	92.06(6)	91.36(3)	91.60(7)
				O7–M1–O8	91.18(7)	91.91(2)	92.38(8)
				O7–M1–O5	85.19(6)	91.95(3)	86.64(7)
				O7–M1–N1	168.32(6)	166.73(3)	166.95(7)
				O8–M1–O5	88.97(6)	85.88(2)	88.85(7)
				O8–M1–N1	100.31(6)	101.14(3)	100.46(7)
				O5–M1–N1	90.79(6)	91.39(3)	91.26(7)

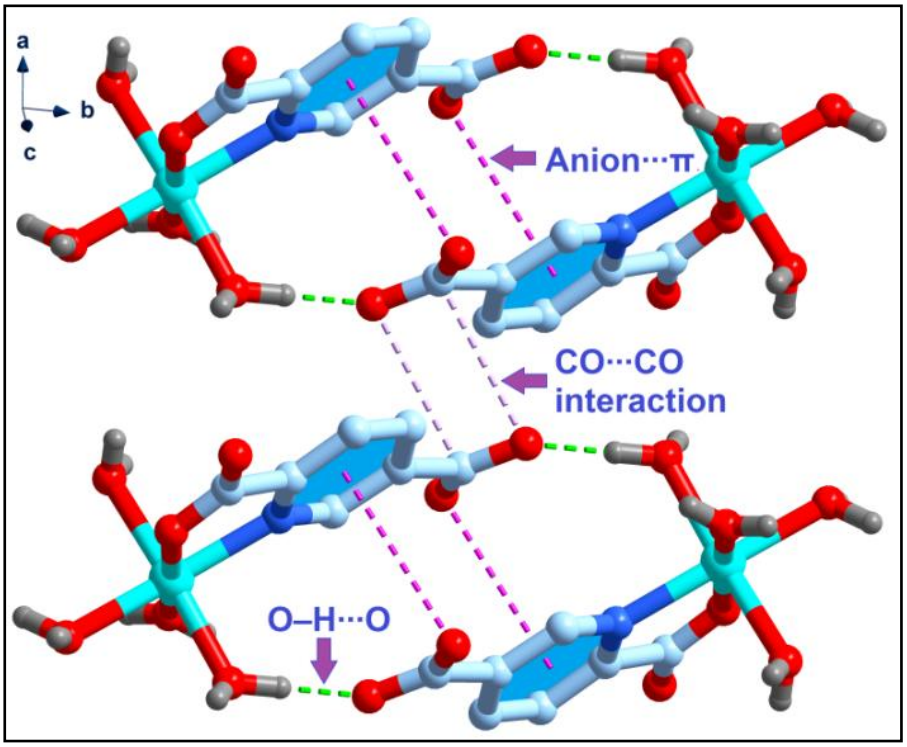

Figure 2.8 Anion···π, CO···CO and O–H···O interactions between two monomeric units of $[Co(2,5\text{-PDC})(H_2O)_4]\cdot 2H_2O$ (**1**).

In the crystal structure of **1**, hydrogen bonding as well as anion···π interaction is observed between the neighbouring monomeric units (**Figure 2.8**). The details of hydrogen bonding geometry are presented in **Table 2.3**. The O4 atom of carboxyl

moiety of *2,5-PDC* of one of the monomeric units is involved in anion···π interactions with the π-system of the *2,5-PDC* of adjacent neighbouring monomeric unit (**Figure 2.8**). The distance between the uncoordinated carboxylate oxygen O4 and the centroid of the *2,5-PDC* ring is 3.595 Å [C6···Cg = 3.812 Å, where Cg is the centroid of the ring defined by atoms N1, C2–C5, C7]. The angle between the O4, the ring centroid and the aromatic plane is 91.03(2)º, which is close to the ideal value of 90° and thus indicative of strong anion···π interaction between the monomeric units.[53] P. Manna *et al.* have shown the importance of such anion···π interactions in crystal packing of various Co(II) complexes.[54] In addition, unconventional anti-parallel CO···CO interactions are also observed between adjacent monomeric units at a C···O distance of 3.301 Å. This distance is found to be a bit longer than the corresponding distance in various reported compounds.[55]

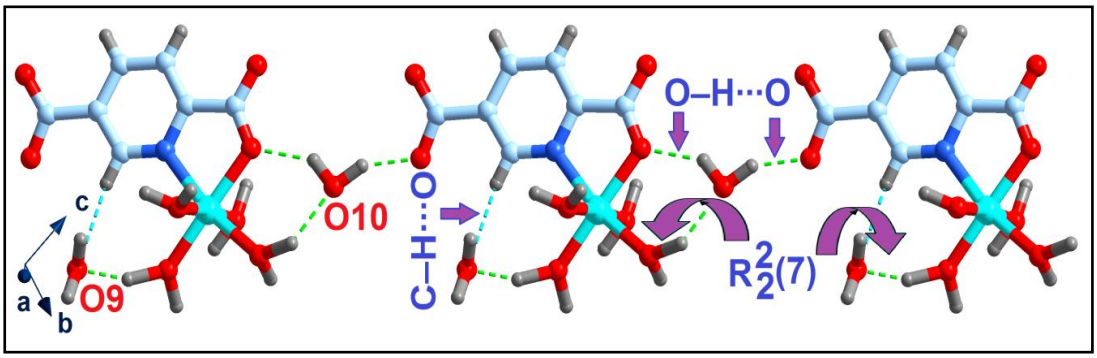

Figure 2.9 1D chain of $[Co(2,5\text{-}PDC)(H_2O)_4]\cdot 2H_2O$ (**1**) assisted by O–H···O hydrogen bonds along with C–H···O interactions.

The coordinated as well as lattice water molecules along with coordinated and uncoordinated carboxylic O atoms of *2,5-PDC* group participate in the formation of hydrogen bonds in **1**. The lattice water (O10) molecules interconnect the neighbouring molecules by two O–H···O hydrogen bonds involving the coordinated carboxylic O (O1) atom of *2,5-PDC* moiety from one monomeric unit and uncoordinated carboxylic O (O4) atom of the another monomeric unit of *2,5-PDC* moiety along the *c* axis resulting in 1D hydrogen-bonded chain (**Figure 2.9**). A six member supramolecular ring motif having Etter's[56] graph-set notation, $R_2^2(6)$ is formed between pairs of lattice and coordinated H_2O molecules via hydrogen bonding interactions involving O10–H10A···O1 and O10–H10B···O4 (**Table 2.3**). The other lattice water molecule (O9)

assists this 1D chain via O8–H8B···O9 and C7–H7···O9 interactions with donor–acceptor distances of 2.716(1) and 2.737(2) Å respectively.

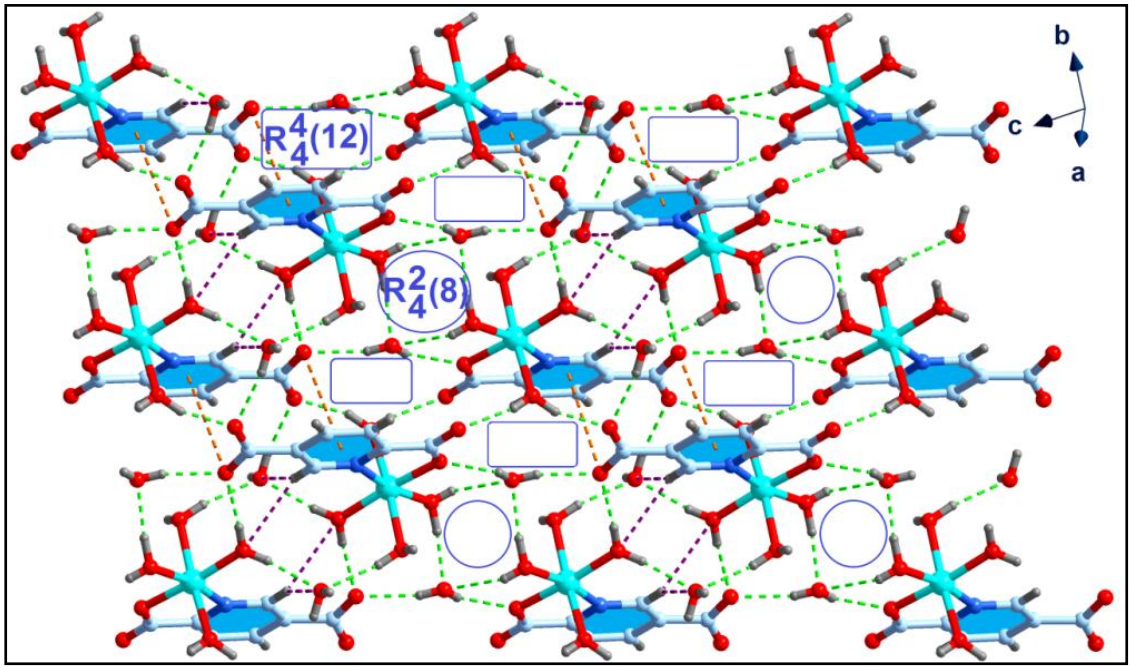

Figure 2.10 Formation of two-dimensional supramolecular layered assembly generated through $R_4^2(8)$and $R_4^4(12)$ hydrogen bonding synthons.

The 1D chains are interconnected along *a* direction by a number of supramolecular contacts, resulting in supramolecular layered architecture in the *ac* plane (**Figure 2.10**). Two adjacent 1D chains are connected by self-complementary O–H···O hydrogen bonds formed between the lattice water (O10) and coordinated water molecule (O7), generating a centro-symmetric $R_4^2(8)$ ring. A third chain connects to them via the involvement of the coordinated water molecule (O5) to give another $R_4^4(12)$ ring. This two types of $R_4^2(8)$and $R_4^4(12)$ rings in **1** repeats along *c*-direction to complete the supramolecular framework in the *ac* plane. Additional reinforcement within this molecular framework is provided by O–H···O, C–H···O and CO(anion)···π interactions. The aqua O8 atom in the molecule acts as a donor to the lattice water molecule (O9), which in turn acts as a donor to the aqua O8 atom with O–H···O distances 1.915 and 1.986 Å respectively. Similarly, pyridyl atom C7 from one chain acts as donor to the same aqua O8 atom from an adjacent chain to give C–H···O interaction at donor–acceptor distance of 3.416(1) Å. The lattice water molecules

extends the 1D chain of monomeric units of compound **1** along the *ac* plane generating the overall 2D supramolecular architecture (**Figure 2.10**). Complex **1** thus, clearly illustrates how lattice water molecules play an important role in stabilizing the metal organic hybrid frameworks.

The lattice water (O9) molecule is responsible for the 3D framework of **1**. Like the other lattice water (O10) molecule, it also acts as a bifurcated acceptor for hydrogen bonds from the coordinated water (O6 and O8) molecules to form intermolecular O6–H6A···O9 and O8–H8B···O9 hydrogen bonds. It connects four neighboring molecules of **1** from different layers that result in a 3D architecture in the crystal structure (**Figure 2.11**).

Compared with **1**, complexes **2** and **3** also show similar networks. However, subtle structural differences between **1**, **2** and **3**, such as bond distances/angles, hydrogen bonds and torsion angles may be due to the different atomic radii of Co(II)/Mn(II)/Zn(II) ions. Theoretical studies on (*vide infra*)[57] interesting assemblies for **1** justify the role of non-covalent interactions in stabilizing its 2D network structure.

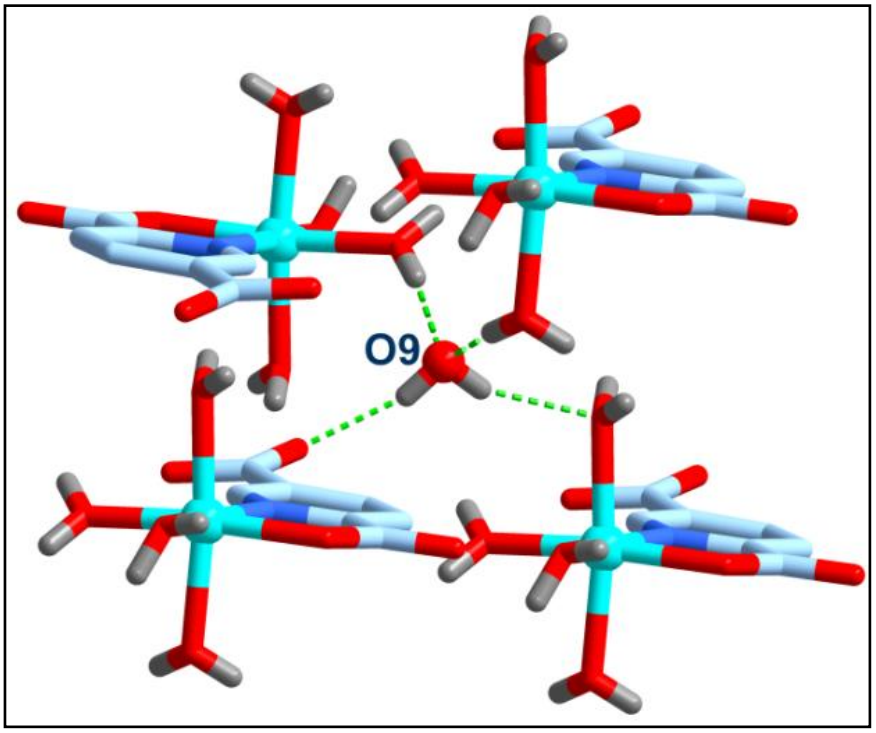

(**a**)

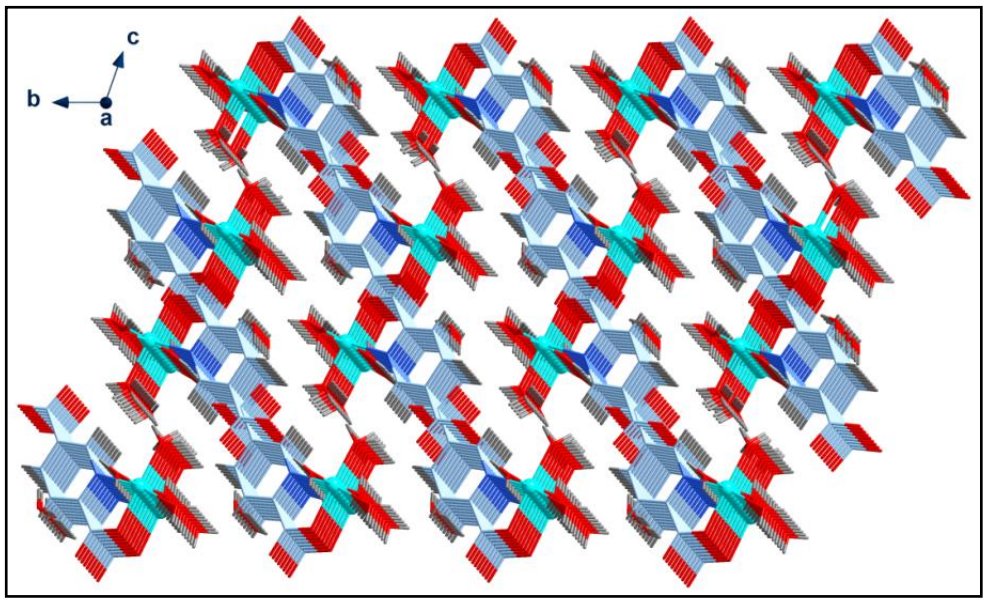

(**b**)

Figure 2.11(**a**) Role of lattice water (O9) molecule in the crystal structure of **1** (Aromatic hydrogen atoms are omitted for clarity). Molecules from different layers are represented by different colors of the central metal ion. (**b**) The hydrogen-bonded 3D architecture of **1**.

Table 2.3 Selected hydrogen bond distances (Å) and angles (°) for **1**, **2** and **3**.

Geometry	D–H···A	d(D–H)	d(D–A)	d(H···A)	<(DHA)	Symmetry code
1D	O10–H10B···O1	0.779	2.764	2.070(1)	148.36(3)	–x,–y,–z
	O7–H7B···O10	0.715	2.833	2.195(1)	149.44(3)	–x,–y,–z
	O7–H7A···O10	0.923	2.738	1.818(0)	175.13(3)	x,+y–1,+z
	O5–H5A···O2	0.712	2.681	1.982(1)	166.96(3)	–x,–y,–z
2D	O10–H10A···O4	0.774	2.729	1.969(1)	167.14(2)	–x+1,–y+1,–z+1
	O8–H8A···O4	0.82	2.679	1.863(0)	172.83(3)	–x+1,–y,–z+1
	O5–H5B···O3	0.898	2.659	1.795(1)	160.67(2)	–x+1,–y+1,–z+1
3D	O6–H6A···O9	0.866	2.953	2.111(1)	164.10(2)	–x+1,–y,–z+1
	O8–H8B···O9	0.806	2.717	1.915(1)	172.99(3)	x, y, z
	O9–H9A···O5	0.785	2.866	2.121(1)	158.58(3)	–x,–y,–z+1
	O9–H9B···O3	0.823	2.785	1.986(0)	163.50(3)	–x+1,–y+1,–z+1

2.3.4 Isostructurality of compounds 1, 2 and 3

It is clear from the above discussion that from the crystallographic point of view, compounds **1**, **2** and **3** are quite analogous, because these three species differ only on the basis of the metal ions present in them. Such structurally related compounds belong to the same structure type and may be termed as isostructural.

The isostructurality of the three crystals has also been evaluated according to the approach of Fábián & Kálmán[58] in which two structures may be compared by a parameter called unit cell similarity index, given by

$$\Pi = [(a+b+c)/(a'+b'+c')] - 1 \text{ where, } (a+b+c > a'+b'+c')$$

Here, *a*, *b*, *c* and *a*′, *b*′, *c*′ are the orthogonalized lattice parameters of the structures being examined. If the structural similarity is very high, the Π value is expected to be practically equal to zero.[58] For compounds **1** and **2**, the value is found to be 0.0009, which corroborates the close structural similarity obtained from crystal structure analyses. The corresponding values for the structure pairs (**1**)/(**3**) and (**2**)/(**3**) are found to be 0.0003 and 0.0003 respectively. The other two related parameters *viz.* mean elongation value ($\in$) and the so-called asphericity index (*A*) of the compounds have also been determined. The $\in$ value describes the difference in cell size;

$$\in = (V' - V)^{1/3} - 1,\ V' > V.$$

Where, *V* and *V*′ are the volumes of the respective unit cells. For our structure pairs (**1**)/(**2**), (**1**)/(**3**) and (**2**)/(**3**), the difference in cell size ($\in$) values estimated are 0.0006, 0.0026 and 0.0006 respectively. Closer the value of $\in$ to zero, higher is the degree of similarity of the structures. On the other hand, asphericity index (*A*) accounts for the shape distortions, and is defined as,

$$A = (2/3)[1 - \sum_{j>i}\{[(1+\in)M_i - 1] \times [(1+\in)M_j - 1]/3\in^2\}]^{1/2}$$

Where, M_i's are the principal axes of matrix M, which gives the pure shear component of the transformation between the two crystallographic coordinate systems. The *A* values for the same structure pairs, *viz*. (**1**)/(**2**), (**1**)/(**3**) and (**2**)/(**3**) are found to be 2.4141, 1.2005 and 1.0997 respectively. In this regard, we can also express their product $\in A$ as the lattice distortion index and the observed values are 0.001452, 0.00316, and 0.00072 respectively.

The above quantities obtained for **1**, **2** and **3** clearly indicate the isostructurality of the three crystalline solids.

2.3.5 Powder X-ray Diffraction

In order to prove that the synthesized M(II) *2,5-PDC* coordination compounds [M = Co(**1**), Mn(**2**), Zn(**3**)] are true representative of their bulk materials, powder X-ray

diffraction of the compounds **1**, **2** and **3** were recorded at room temperature. The experimental and the calculated powder X-ray diffraction patterns for compounds **1** and **2** (see **Figures 2.12-2.13**) are in agreement with each other, which demonstrates that the compounds are true representatives of the bulk samples prepared by us. The small line width of the Bragg reflections demonstrates the good crystallinity of the compounds. Furthermore, the perfect fit of the lines indicates in favour of the closeness of the unit cell linear parameters.[59] Small differences in reflection intensities and peak positions are observed between the simulated and experimental patterns, which can be attributed to the variation in crystal orientation or particle size of the powder sample.[60] The powder X-ray diffraction pattern of compound **3** (**Figure 2.14**) displays significant deviations from the simulated one. This observation can be attributed to the routine sample preparation process.[61] It is also possible that phase transformation of compound **3** occurs due to grinding prior to PXRD measurement.[61]

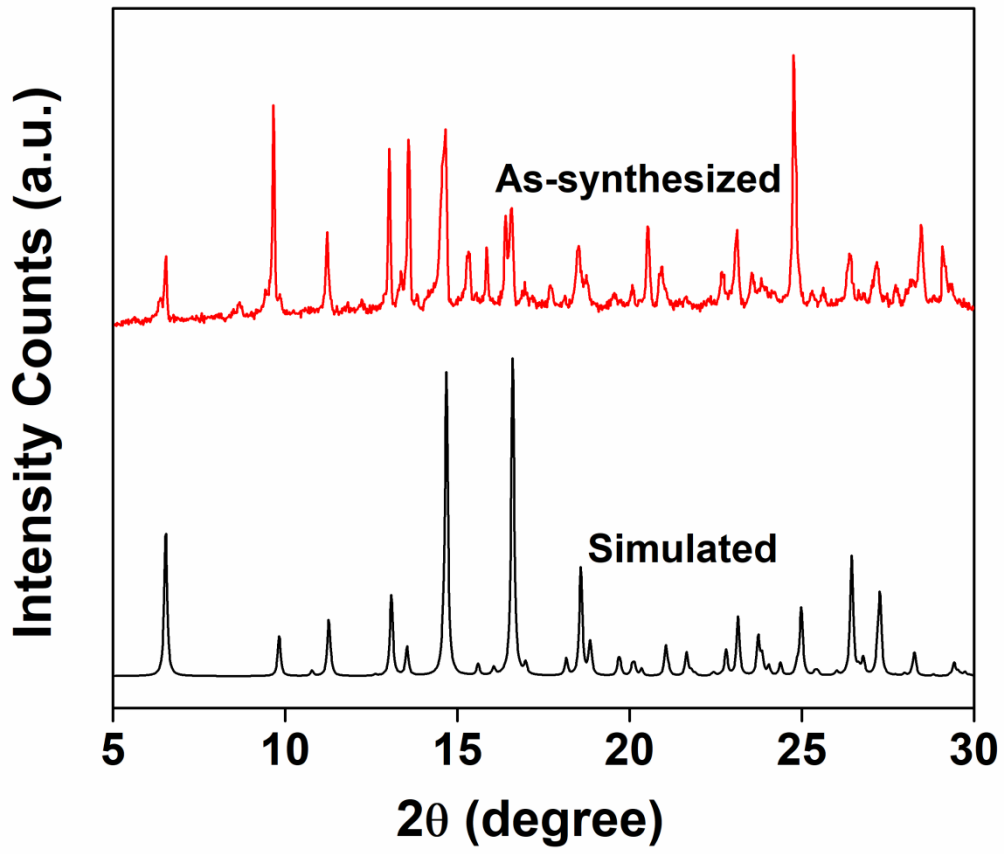

Figure 2.12 Powder X-ray diffraction patterns: as-synthesized (red) and simulated from MERCURY software (black) of $[Co(2,5\text{-}PDC)(H_2O)_4]\cdot 2H_2O$ (**1**).

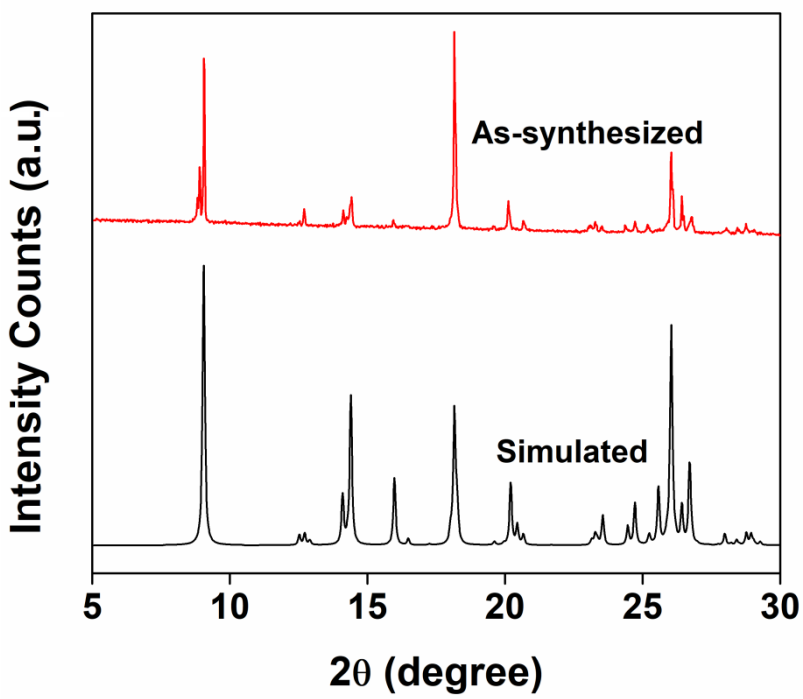

Figure 2.13 Powder X-ray diffraction patterns: as-synthesized (red) and simulated from MERCURY software (black) of $[Mn(2,5\text{-PDC})(H_2O)_4]\cdot 2H_2O$ (**2**).

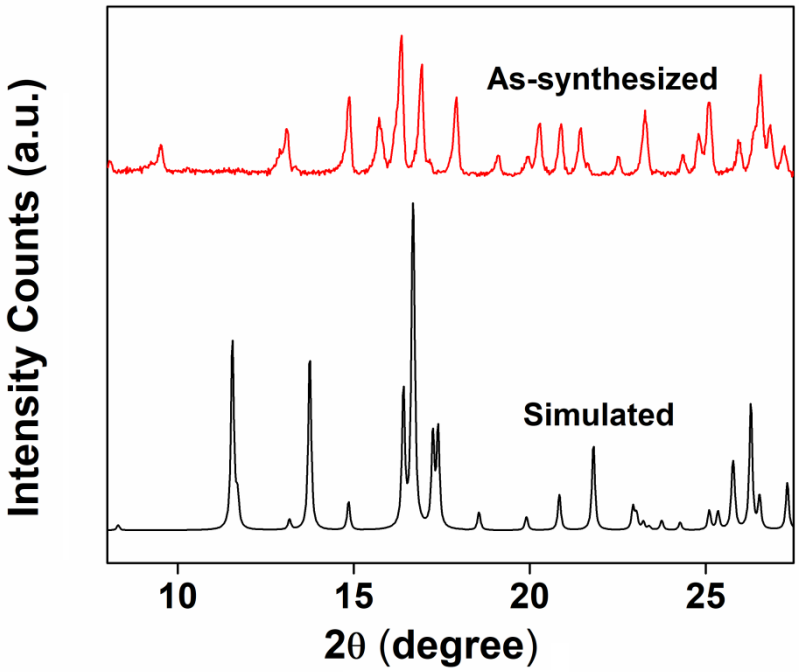

Figure 2.14 Powder X-ray diffraction patterns: as-synthesized (red) and simulated from MERCURY software (black) of $[Zn(2,5\text{-PDC})(H_2O)_4]\cdot 2H_2O$ (**3**).

2.3.6 Theoretical Studies

The theoretical study is devoted to the analysis of the intermolecular anion–π, CO···CO and H-bonding interactions that govern the formation of supramolecular 1D chain in compound **1** as described below. First of all, we have computed the molecular electrostatic potential (MEP) plotted onto the approximate van der Waals surface (isosurface 0.001 a.u.) in order to investigate the electron rich and electron poor region of the molecule (**Figure 2.15**).

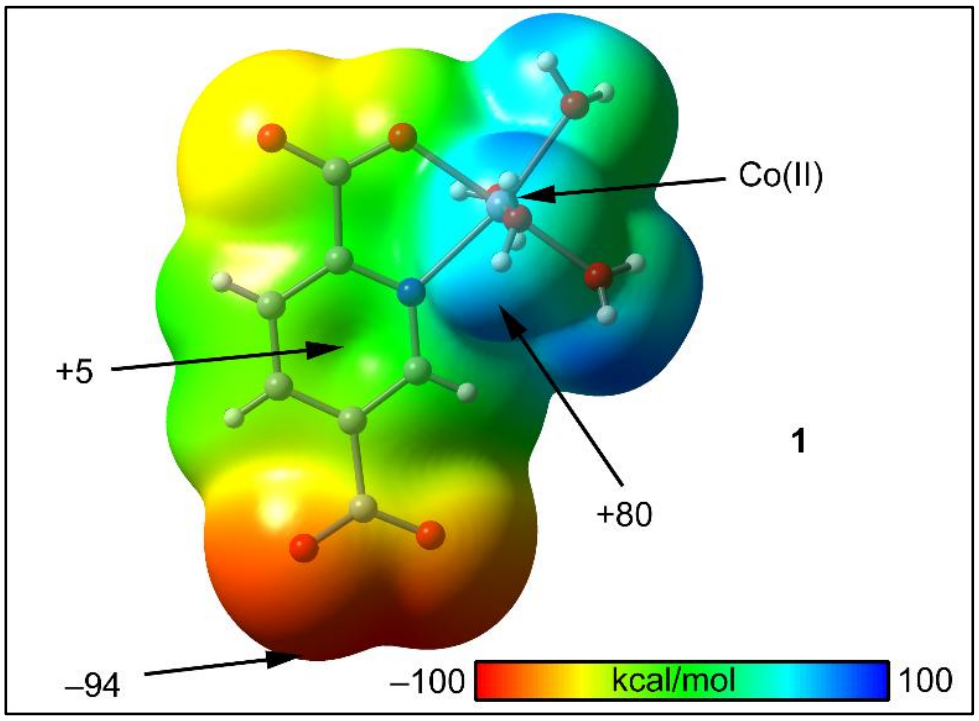

Figure 2.15 MEP surface of compound $[Co(2,5\text{-}PDC)(H_2O)_4]\cdot 2H_2O$ (**1**), isosurface 0.001 a.u. at the M06-2X/def2-TZVP level of theory. The values at selected points of the surface are indicated.

It should be mentioned that both compounds **1** and **2** are zwitterions, with an uncoordinated carboxylate anion on one side of the molecule and the cationic metal center (Co or Mn) on the opposite side. Therefore, the most positive region is located at the protons of the coordinated water molecules. The most negative region is located at the O-atoms of the carboxylate group (–90 kcal/mol), as expected. Therefore, the most favored interaction from an electrostatic point of view is an H-bond between the M–OH and the carboxylate group. Moreover, the inspection of the MEP surface also reveals

that the MEP above the aromatic ring is slightly positive (+5 kcal/mol), thus adequate for establishing π-interaction with electron rich atoms.

Figure 2.16(a) shows a partial view of the X-ray structure of compound **1** (H-atoms omitted), that we have selected as a model of both complexes to analyze the infinite 1D supramolecular chain that is generated in their solid state X-ray structure. This supramolecular chain is formed by the propagation of the self-assembled dimers (described above in **Figure 2.8**) in crystallographic *a* direction by means of anti-parallel CO···CO interactions [highlighted in green in **Figure 2.16(a)**]. This type of interaction has been previously described and studied in terms of geometries and energies.[62] Three such common interaction motifs are observed in crystal structures: (a) a slightly sheared antiparallel motif (involving a pair of short C···O interactions, the most frequent), (b) a perpendicular motif and (c) a highly sheared parallel motif which involves a single C···O interaction (less frequent). Combined theoretical and crystallographic studies have shown that the C···O distance ranges from 2.92-3.32 Å.[21] In compound **1**, the C···O distance is 3.30 Å, just in the upper limit, therefore, the interaction is expected to be weak. In **Figure 2.16(b)**, we represent the H-bonded self–assembled dimer, where in addition to the H-bonds; two symmetrically equivalent anion–π interactions (Aπ) are also established. The interaction energy of this dimer is very large (ΔE_1 = –67.3 kcal/mol) due to the combination of both interactions that are established between the most electron rich and electron poor groups, as shown by the MEP surface in **Figure 2.15**. In **Figure 2.16(c)**, we show the dimer extracted from the infinite supramolecular chain where the antiparallel CO···CO interaction is formed. The dimerization energy is ΔE_2 = –7.9 kcal/mol which is slightly stronger than previous reports on CO···CO n→π* interactions. For instance, it has been reported a binding energy of –5.4 kcal/mol for the *bis*-propanone dimer.[21] In case of Mn instead of Co (compound **2**), the interaction energy is slightly stronger (ΔE_2 = –8.7 kcal/mol), in agreement with the shorter C···O distance observed for Mn (3.29 Å).

In order to further characterize the non-covalent interactions commented above, we have used the NCI plot index computational tool. Non-covalent interactions are efficiently visualized and identified by using the NCI plot tool. It allows an easy assessment of host-guest complementarity and the extent to which weak interactions stabilize a complex. **Figure 2.17(a)** shows the NCI plot obtained for the H-bonded self-

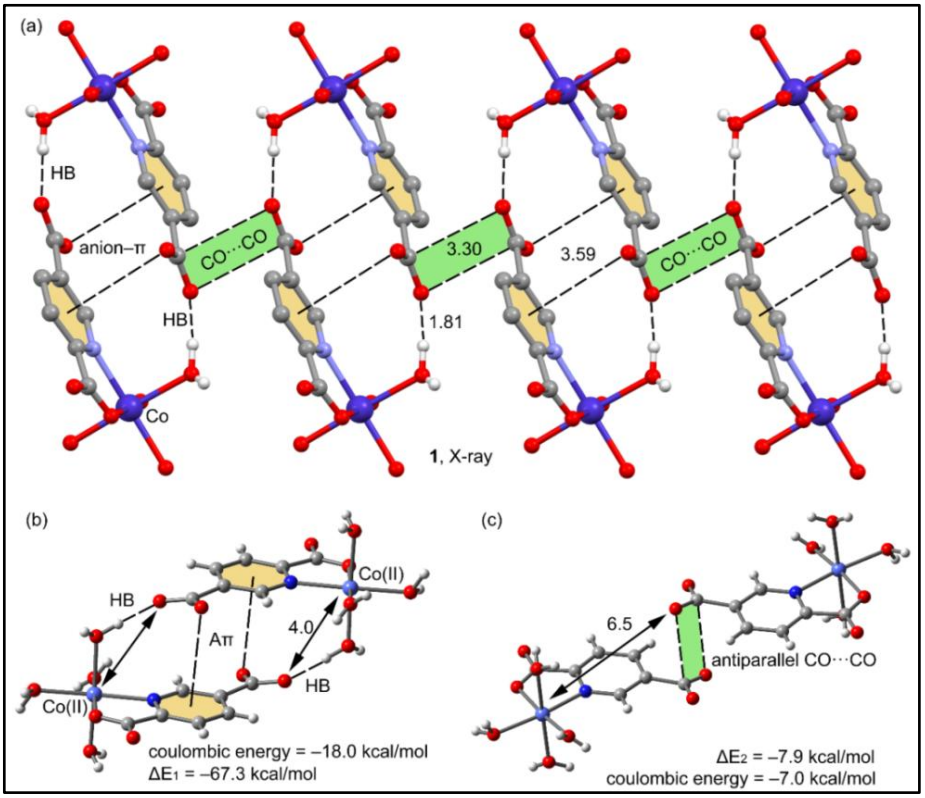

Figure 2.16(**a**) Partial view of the X-ray structure of compound **1**. H-atoms are omitted for clarity apart from those of the coordinated water molecule that establish the O–H···O interactions. (**b**, **c**) Theoretical models used to evaluate the non-covalent interactions. Distances in Å.

assembled dimer. It can be observed that the presence of two small and strong blue isosurfaces characterize the intermolecular H-bonds, which indicates that they are very strong, in agreement with the MEP analysis and interaction energies. In addition, more extended and green isosurfaces are located between the carboxylate and the aromatic rings confirming the existence of the anion–π interactions. We have used the quantum theory of "atoms-in-molecules" and the value of the kinetic $G(r_{CP})$ contribution to the local energy density of electrons at the critical point (CP) to calculate the energies for each individual H-bonding contact. It has been calculated according to the conventional approach by Vener *et al.*[63] that was specifically developed for HBs [Energy = 0.429 * G(r) at the bond CP]. The latter method is convenient to know the individual contribution of each contact and also to evaluate the influence of the H-bonding in the

presence of other interactions. By using this formula, each H-bond accounts for –8.6 kcal/mol. In **Figure 2.17(b)**, we have represented the NCI plot of the other dimer (CO···CO interaction). It can be clearly observed the presence of a green isosurface between both CO groups, thus confirming both the existence and the weak nature of the interaction, in agreement with the energetic results.

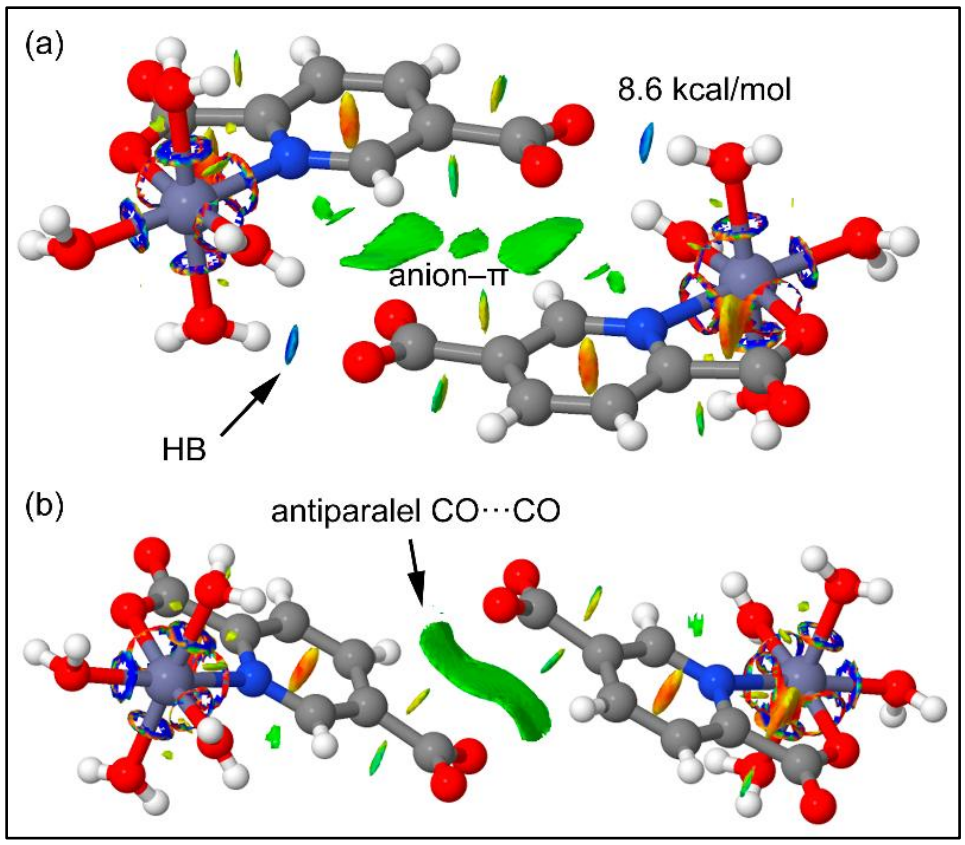

Figure 2.17(a) NCI plot of the self-assembled H-bonded dimer in [Co(2,5-PDC)$(H_2O)_4]\cdot 2H_2O$ (**1**). (**b**) NCI plot of the antiparallel CO···CO H-bonded dimer in [Co(2,5-PDC)$(H_2O)_4]\cdot 2H_2O$ (**1**). The gradient cut-off is $s = 0.35$ a.u. and the color scale is $-0.04 < \rho < 0.04$ a.u.

2.3.7 Thermal studies

The thermogravimetric (TG) analyses of compounds **1**, **2** and **3** were carried out in the temperature range of 25-700°C under N_2 atmosphere at the heating rate of 10°C min^{-1} (**Figure 2.18**). The iso-structural complexes exhibit almost similar thermal decomposition patterns. For complex **1**, the first weight loss of 19.08% between 48-128°C is attributable to the loss of two lattice as well as two coordinated water

molecules (calculated 21.64%). The second weight loss occurs from 130-205°C, attributed to loss of the remaining two coordinated water molecules (observed weight loss 8.80%; calculated 10.82%).[64] The weight loss corresponds to 343-685°C can be attributed to the breakdown of *2,5-PDC* moiety (observed weight loss 49.34%; calculated 49.71%).[65] Similar thermal decomposition of *2,5-PDC* moiety has also been observed for cadmium(II) complex, *viz*. $[Cd(2,5\text{-}PDC)_2(H_2O)_2].H_2O$ involving 3D supramolecular assemblies.[66]

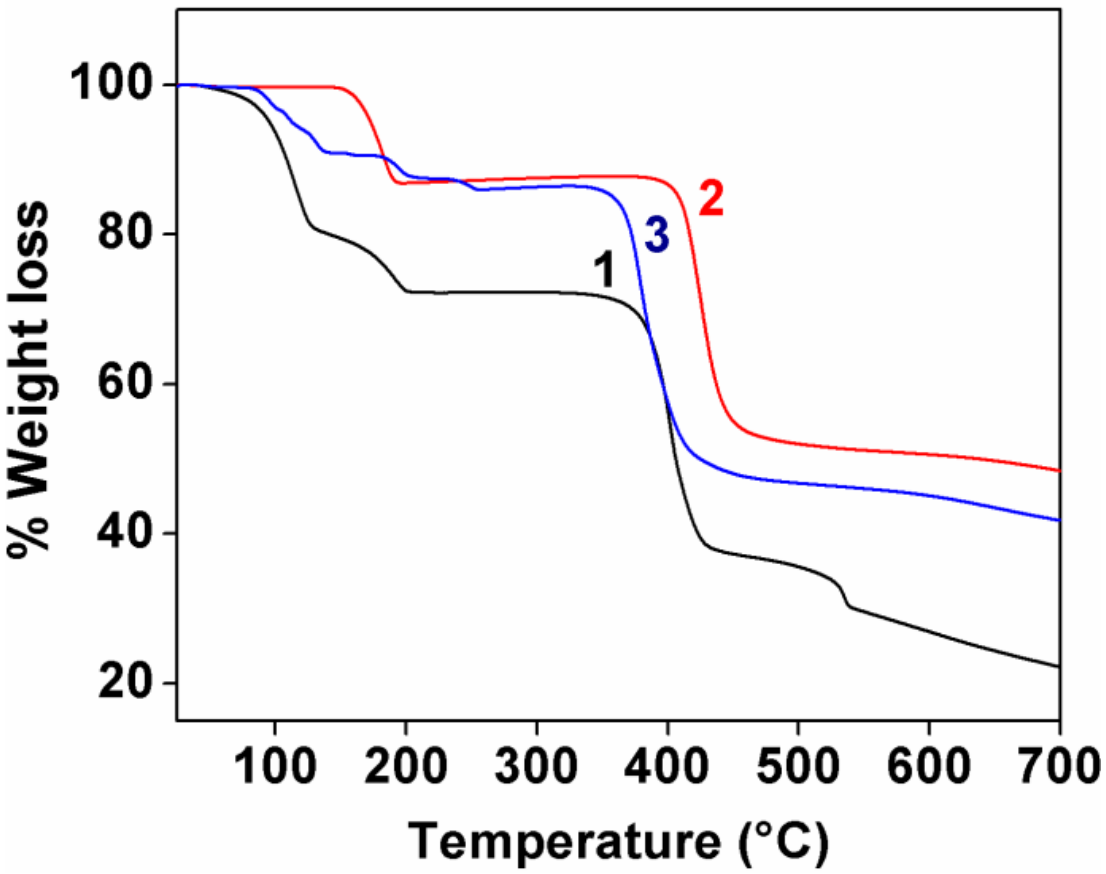

Figure 2.18 TGA curves of compounds **1**, **2** and **3**.

For compound **2**, the 13.11% (calculated 10.98%) weight loss in the temperature range 144-200°C was due to the removal of two lattice water molecules. This is followed by a plateau region from 200-387°C. Thereafter weight loss of 36.67% (calculated 38.26%) occurs in the temperature range of 387-700°C, corresponding to the loss of the two coordinated water molecules along with the breakdown of half of the

2,5-PDC moiety.[67] For **3**, the first weight loss occurring at 97-155°C could be assigned to the removal of the two lattice water molecules (observed weight loss 9.19%; calculated 10.64%). A negligible weight loss of 6.16% was thereafter observed at 194-269°C (calculated 5.32%), corresponding to the removal of one coordinated water molecule. Such a high temperature of the coordinated solvent molecule departure indicates a strong bonding interaction between the aqua molecule and the metal centre. This was followed by a dramatic weight loss of 42.88%, starting from 350 to 700ºC (calculated 44.34%). It could be attributed to loss of the remaining three coordinated water molecules along with the breakdown of half of the *2,5-PDC* moiety.[67]

2.3.8 Cell viability and apoptosis assay

MTT assay is a widely accepted method for measuring cell proliferation or cell cytotoxicity of chemicals/drug molecules and this assay also represents an effective method for the development of new metal-based cytotoxic drug candidate(s).[68] The cell viability results obtained for compounds **1** and **2** on DL cell line treated for 24 hours showed significant decrease ($P \leq 0.05$) in cell viability with insignificant cytotoxic effect against peripheral blood mononuclear cells (PBMC). The different dose applied and the relative cell viability percentage obtained for each compound along with reference drug are then inserted into the statistical software namely GraphPad Prism to determine the IC_{50} values (concentration required for 50% inhibition of cell viability) based on a nonlinear regression of a variable slope model.[69] The IC_{50} of the compounds compared to the reference drug is shown in **Table 2.4**. The analyses of mean IC_{50} using above mentioned method obtained for cisplatin, compounds **1** and **2** were 0.45, 32.2 and 26.3 μM respectively (**Figure 2.19** and **Table 2.4**). Nevertheless, this method does not provide any information regarding the mechanism associated with cell death, the phase in the cell cycle that is affected by the drug as well as related biological targets. For these purposes additional methods, such as acridine orange and ethidium bromide (AO/EB) based apoptosis study was carried out in DL cells. Compounds **1** and **2** mediated apoptosis induction was studied by means of AO/EB dual staining method followed by morphological analysis of nuclei after exposure to different concentrations (0.5, 1 and 5 μM) (**Figure 2.19**).

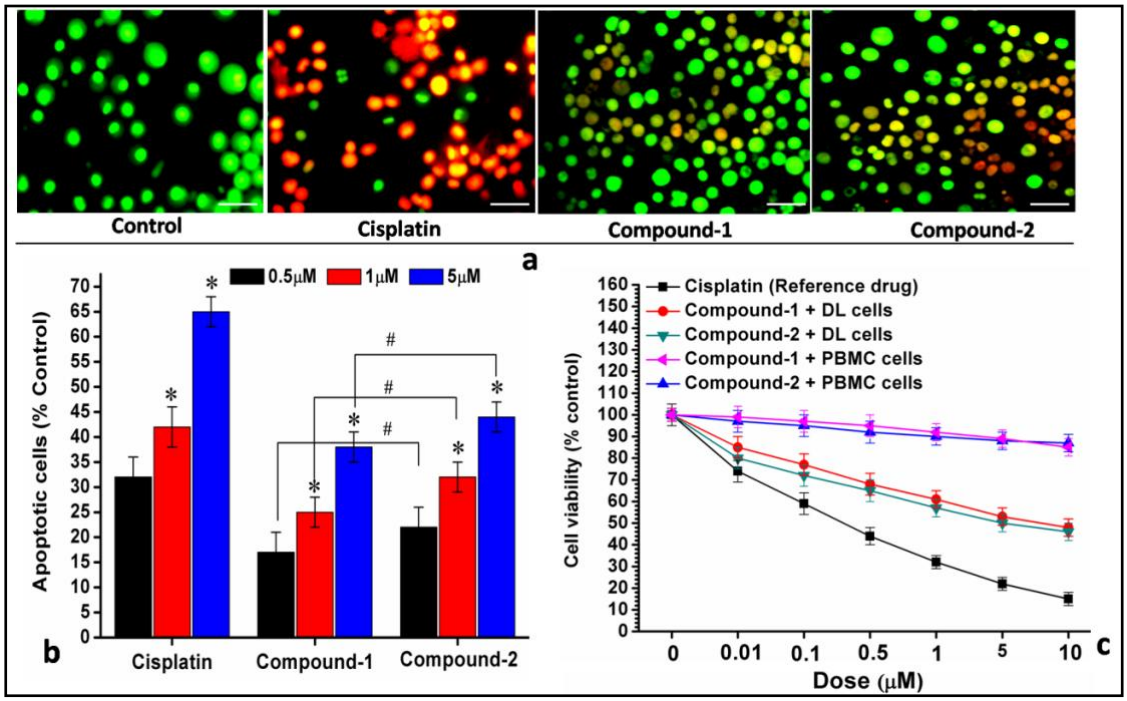

Figure 2.19 Compounds $[Co(2,5\text{-}PDC)(H_2O)_4]\cdot 2H_2O$ (**1**) and $[Mn(2,5\text{-}PDC)(H_2O)_4]\cdot 2H_2O$ (**2**) mediated cytotoxicity and apoptotic cell death in DL and PBMC cells (**a**) morphological features of apoptotic and viable cells with acridine orange and ethidium bromide (AO/EB) staining. Control DL cells showed mostly viable cells, cisplatin and complex $[Co(2,5\text{-}PDC)(H_2O)_4]\cdot 2H_2O$ (**1**) treated groups showing apoptotic features evident by red/orange nuclei with membrane damage and blebbing. Scale bar 10 μm. (**b**) showed percentage apoptotic cells after treatment with the compounds and the reference drug cisplatin at different dosage. (**c**) Compounds $[Co(2,5\text{-}PDC)(H_2O)_4]\cdot 2H_2O$ (**1**) and $[Mn(2,5\text{-}PDC)(H_2O)_4]\cdot 2H_2O$ (**2**) induced cytotoxicity in DL and PBMC cells. Data are mean ± S.D., n = 3, ANOVA, $P \leq 0.05$.

Control group showed viable DL cells identified by bright uniform green nuclei with organized structures. Compounds **1** and **2** treated cells showed concentration-dependent increase in apoptotic features in DL cells such as nuclear marginalization and chromatin condensation, fragmented nuclei, cytoplasmic vacuoles and scattered apoptotic bodies (under 100x resolution). Although, AO-EB and the MTT assays showed similar dose-dependent effects on DL cell viability, the percentage of viabilities were different. In MTT assays, absorbance of control cells were considered as 100% and percentages of viable cells were calculated as ratio to the control, while in AO/EB assay, percentage of viable cells (green nuclei) are real numbers, calculated as ratio to the total number of cells (green and red nuclei) during treatment.[70] The differences in

the cell viability during MTT assay and apoptosis can be considered to be due to early detection of cell death caused by mitochondrial function (MTT assays); measuring apoptosis indicating assays (AO-EB) detect cell death latter in the process.[71] MTT and apoptosis assays reveal that both the compounds **1** and **2** have antiproliferative properties and compound **2** shows better antiproliferative activity than the compound **1** with lower IC_{50} values resulting in a higher percentage of apoptotic cells after 24 hours of exposure.

Table 2.4 IC_{50} values of cisplatin, compounds **1** and **2** on DL and PBMC cells.

Sl nos.	Reference drug/Compounds	IC_{50} (μM) DL cells (Cancer cells)	PBMC (Normal cells)
1	Cisplatin	0.45	06.31
2	Compound **1**	32.2	137.13
3	Compound **2**	26.3	117.13

2.3.9 Molecular Docking studies

To corroborate the fluorescence based apoptosis study as well as the observed cell cytotoxicity and apoptotic cell death (significantly high) induced by both compounds in DL cells, we have performed *in silico* molecular docking simulations to understand the possible interactions between anti-apoptotic proteins and the structures of the compounds under study. Anti-apoptotic proteins such as BCL-2, BCL-XL and MCL-1 interact with pro-apoptotic proteins to initiate the process of apoptosis.[72] BCL-2 family proteins are key regulators of apoptosis process and are classified into three major functional groups: anti-apoptotic proteins such as BCL-2, pro-apoptotic effectors (*BAX*, *BAK* and *BOK*) and pro-apoptotic activators (*BID*, *BIM*, *NOXA*, *BAD* and *PUMA*). Preclinical data suggest that activators, which contain only a single *BH3* motif (*an amphipathic α-helix that interacts with the hydrophobic cleft of anti-apoptotic BCL-2 family proteins*), are important mediators in the cellular response to stresses including DNA damage.[73] Effectors are BCL-2 proteins that are closely associated with the mitochondrial membrane, and when stimulated by *BH3* activators, they promote the formation of pores in the mitochondrial membrane, initiating the apoptotic program.[74]

Over expression (*the abnormal expression of a gene/protein in increased quantity*) of these anti-apoptotic proteins leads to several cancer growth by preventing

apoptosis. A number of studies have recently shed light onto the role of pro- and anti-apoptotic BCL-2 family proteins in tumour-pathogenesis and in mediating the effects of classical as well as novel front-line anticancer agents. This allows the development of more efficient and more precisely targeted cancer treatment regimens.[75] Moreover, their inhibition by various chemotherapeutic agents is associated with the apoptotic induction and hence inhibition of cancer growth and invasion. ABT-199 (*highly specific inhibitor of intracellular interactions with the BCL-2 protein*) received breakthrough therapy designation from the Food and Drug Administration (FDA) due to its apparent efficacy in CLL (*Chronic lymphocytic leukemia*) and AML (*Acute myeloid leukemia*).[76] In this study, docking simulations were performed for anti-apoptotic proteins with compounds **1** and **2**. Our findings show that both the compounds have significantly high binding affinities for BCL-2, BCL-XL and MCL-1 (**Figure 2.20** and **Figure 2.21**). Thus, based on the docking analysis (**Figure 2.22**), both the compounds indicated potential apoptotic inducing ability due to efficient interaction with anti-apoptotic target proteins.

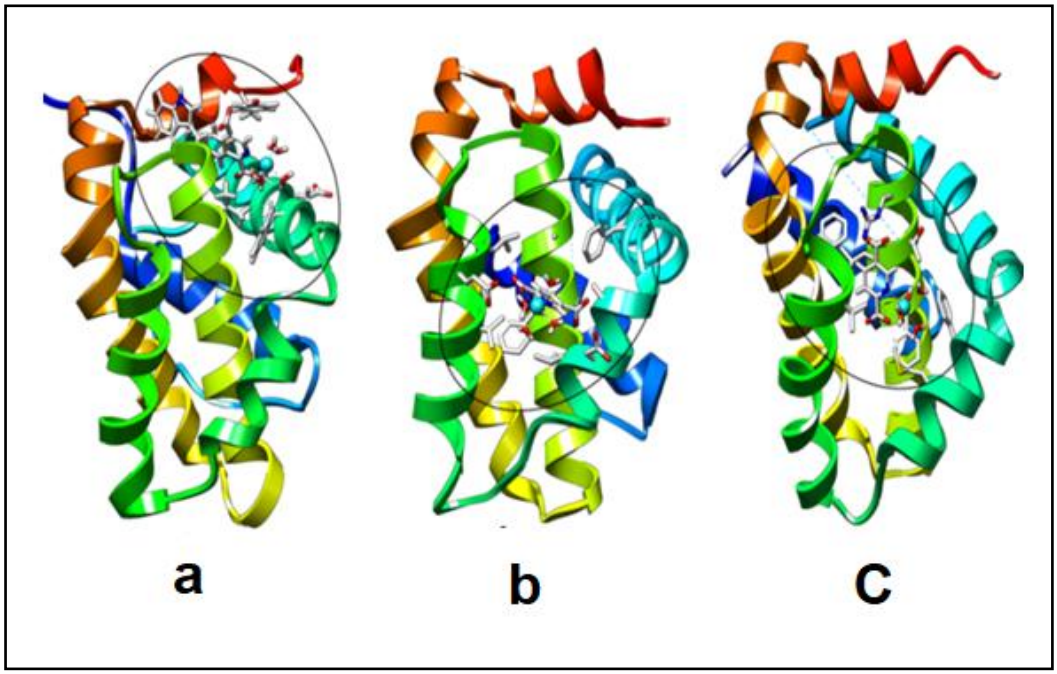

Figure 2.20 Docking structure of $[Co(2,5\text{-}PDC)(H_2O)_4]\cdot 2H_2O$ (**1**) with BCL-2 (PDB: 2O22), BCL-XL (PDB: 2yxj) and MCL-1 (PDB: 5vkc) receptor. (**a**) Ribbon structure of the receptor with compound **1** (**b**) Surface structure of the receptor with compound **1** in active site and (**c**) Hydrogen bonding interactions between receptor and compound **1**. Notation: Dotted line - H-bond.

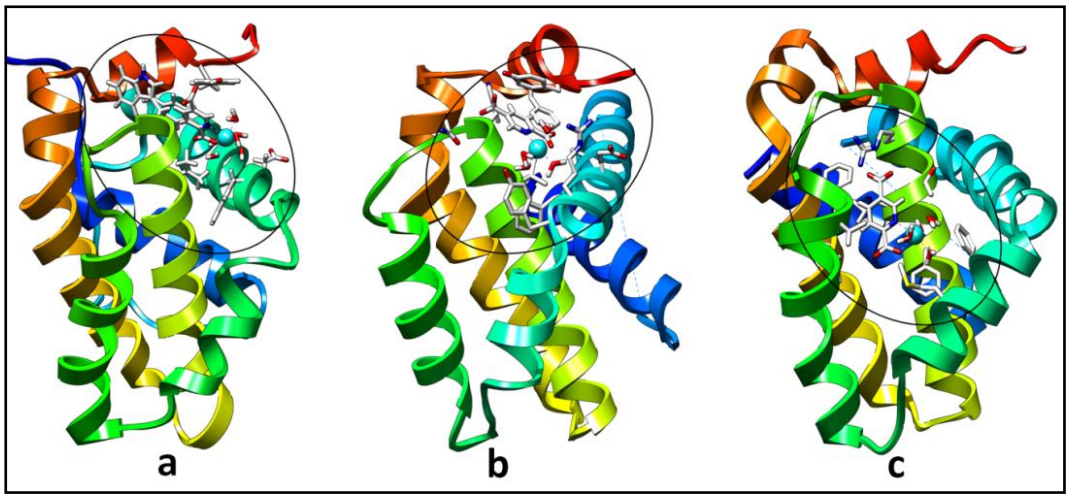

Figure 2.21 Docking structure of compound $[Mn(2,5\text{-}PDC)(H_2O)_4]\cdot 2H_2O$ (**2**) with BCL-2 (PDB: 2O22), BCL-XL (PDB: 2yxj) and MCL-1 (PDB: 5vkc) receptor. (**a**) Ribbon structure of the receptor with compound **2** (**b**) Surface structure of the receptor with compound **2** in active site and (**c**) Hydrogen bonding interactions between receptor and compound **2**. Notation: Dotted line - H- bond.

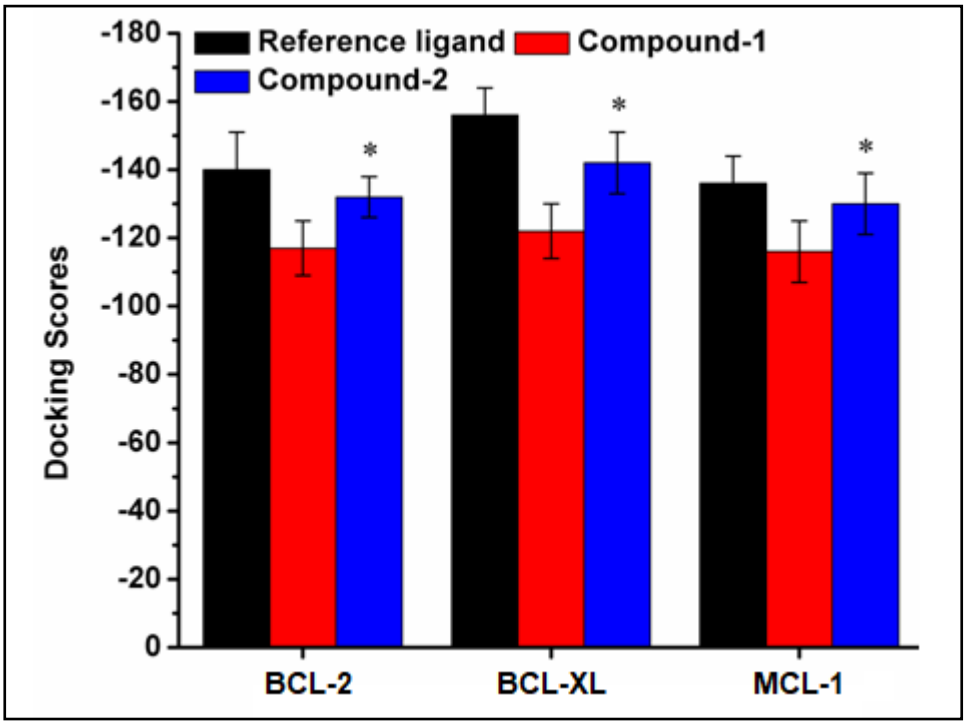

Figure 2.22 Docking scores of $[Co(2,5\text{-}PDC)(H_2O)_4]\cdot 2H_2O$ (**1**) and $[Mn(2,5\text{-}PDC)(H_2O)_4]\cdot 2H_2O$ (**2**) with BCL-2 (PDB: 2O22), BCL-XL (PDB: 2yxj) and MCL-1 (PDB: 5vkc) receptors. As per MVD rerank score algorithm lowest the score better is the interaction. Data are mean ±S.D, n = 3, ANOVA, $P \leq 0.05$.

2.3.10 Pharmacophore modelling

In modern computational and medicinal chemistry, pharmacophore features are useful to identify the essential components of one or multiple molecules with the similar biological activities.[77] It also represents signature of chemical compounds which can be used to search for more molecules which share the same features when arranged with 3D orientations. To be effective as a drug candidate, bioactive compound(s) must reach its target destination and stay in the body without losing potency for the expected biological events to occur. In that context, computer models constitute valid alternatives to experiments. Here, we have identified important pharmacophore features such as hydrophobic, positive and negative ionisable groups that are responsible for biological activities (**Figure 2.23**) of the compounds **1** and **2**.

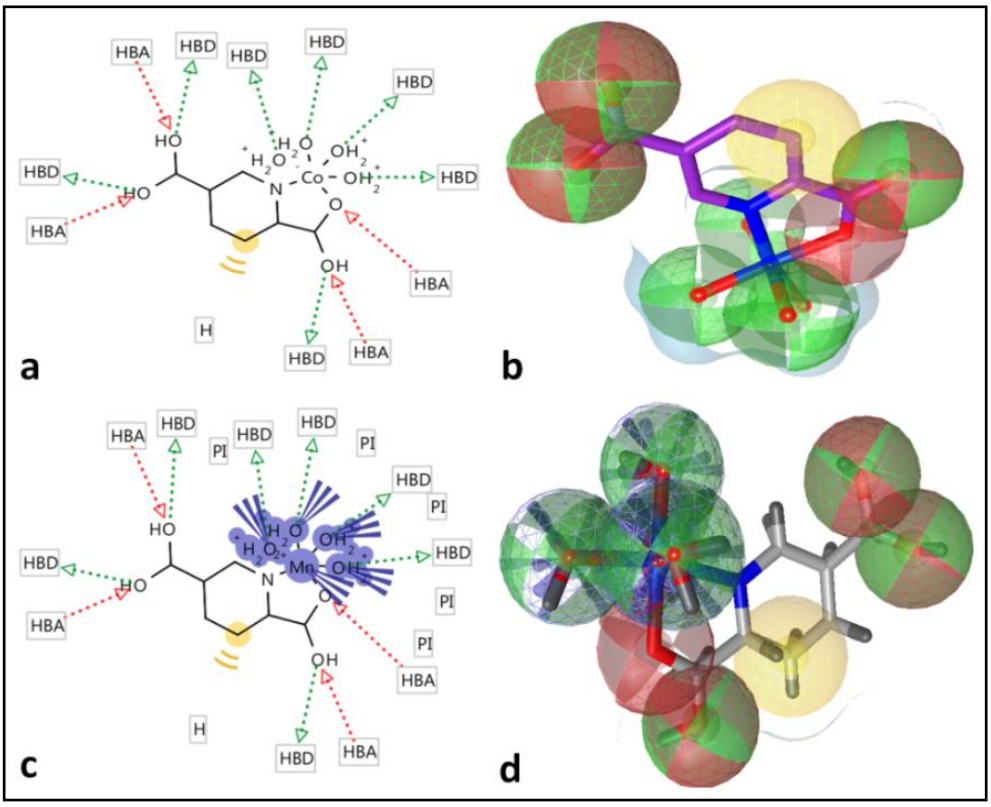

Figure 2.23 Pharmacophore model showing the structural fragments responsible for biological activities of compound $[Co(2,5\text{-}PDC)(H_2O)_4]\cdot 2H_2O$ (**1**) (**a**, **b**) and $[Mn(2,5\text{-}PDC)(H_2O)_4]\cdot 2H_2O$ (**2**) (**c** and **d**). Hydrophobic, positive ionizable, negative ionizable and acceptor interactions are depicted as yellow spheres, blue star, red star and red arrows, respectively.

2.4 CONCLUSIONS

Three isostructural complexes of Co(II), Mn(II) and Zn(II) *viz*. [Co(2,5-PDC)$(H_2O)_4]\cdot 2H_2O$ (**1**), [Mn(2,5-PDC)$(H_2O)_4]\cdot 2H_2O$ (**2**) and [Zn(2,5-PDC)$(H_2O)_4]\cdot 2H_2O$ (**3**) have been successfully synthesized and characterized by single X-ray diffraction, electronic and vibrational spectra, PXRD and TGA. The three isostructural complexes were further characterized by evaluating the isostructurality parameters using Fabian and Kalman approach. O–H···O hydrogen bonding interactions involving the lattice water molecules and anion···π contacts involving carboxylate moiety of *2,5-PDC* of the monomeric units in the crystal structures result in layered networks in all the complexes. We have used the molecular DFT calculations and evaluated energetically the strength of the unusual contacts in complexes **1** and **2**. We have analyzed the CO···CO antiparallel interactions energetically and also by means of the NCI plot analysis tools. The dimerization energy for the dimer extracted from the infinite supramolecular chain involving the antiparallel CO···CO for **1** is ΔE_2 = –7.9 kcal/mol which is slightly stronger than previous reports. In case of compound **2** with Mn(II), the interaction energy is slightly stronger (ΔE_2 = –8.7 kcal/mol); in agreement with its shorter C···O distance. Both the compounds significantly induce cell cytotoxicity in DL cells by inducing apoptotic cell death with negligible cytotoxicity in normal cells. Furthermore, treatment also caused appearance of apoptotic features such as apoptotic bodies, chromatin condensation and membrane blebbing as evident by fluorescence based nuclear morphology studies. The *in silico* molecular docking results reveal that the compounds **1** and **2** fitted well in the inhibitor binding pocket of key target proteins that are reported to be involved in cancer progression and metastasis. Structure activity relationship (SAR) analyses based on pharmacophore modelling reveal that the molecular features of the structures of the compounds **1** and **2** play important role in the biological activities.

REFERENCES

1. (a) Wang, X.; Yao, W.; Qi, Y. F.; Luo, M. F.; Wang, Y. H.; Xie, H. W.; Yu, Y.; Ma, R. Y.; Li, Y. G. *CrystEngComm.* **2011**, *13*, 2542.

(b) Zhu, Y. P.; Ma, T. Y.; Liu, Y. L.; Ren, T. Z.; Yuan, Z. Y. *Inorg. Chem. Front.* **2014**, *1*, 360.

(c) Maspoch, D.; Ruiz-Molina, D.; Veciana, J. *Chem. Soc. Rev*. **2007**, *36*, 770.

(d) Robin, A. Y.; Fromm, K. M. *Coord. Chem. Rev*. **2006**, *250*, 2127.

(e) Xue, X.; Wang, H.; Hana, Y.; Hou, H. *Dalton Trans*. **2018**, *47*, 13.

(f) Andruh, M.; *Chem. Commun*. **2018**, *54*, 3559.

(g) Chandra, R.; Ghorai, A.; Patra, G. K. *Sensor Actuat. B-Chem*. **2018**, *255*, 701.

2. (a) Zhang, Z.; Zhao, H.; Matsushita, M. M.; Awaga, K.; Dunbar, K. R. *J. Mater. Chem*. **2014**, *2*, 399.

(b) Park, I. H.; Chanthapally, A.; Zhang, Z.; Lee, S. S.; Zaworotko, M. J.; Vittal, J. J. *Angew. Chem. Int. Ed.* **2014**, *53*, 414.

(c) Batten, S. R.; Robson, R. *Angew. Chem. Int. Ed.* **1998**, *37*, 1460.

3. (a) Gangu, K. K.; Mukkamala, S. B. *Synth. React. Inorg*. **2016**, *46*, 98.

(b) Gangu, K. K.; Dadhich, A. S.; Mukkamala, S. B, *J. Chem. Sci*. **2015**, *127*, 2225.

(c) Liu, C. B.; Cong, Y.; Sun, H. Y.; Che, G. B. *Inorg. Chem. Commun*. **2014**, *47*, 71.

(d) Soudani, S.; Hajji, M.; Mi, J. X.; Jelsch, C.; Lefebvre, F.; Guerfel, T.; Nasr, C. B. *J. Mol. Struct*. **2020**, *1199*, 127015.

(e) Etaiw, S. E. H.; El-bendary, M. M. *J. Mol. Struct*. **2018**, *1173*, 7.

4. Gangu, K. K.; Maddila, S.; Mukkamala, S. B.; Jonnalagadda, S. B. *Inorg. Chim. Acta* **2018**, *482*, 830.

5. (a) Liu, F. Q.; Wang, Q. X.; Jiao, K.; Jian, F. F.; Liu, G. Y.; Li, R. X. *Inorg. Chim. Acta* **2006**, *359*, 1524.

(b) Moncol, J.; Korabik, M.; Segla, P.; Koman, M.; Miklos, D.; Jaskova, J.; Glowiak, T.; Melnik, M.; Mrozinski, J.; Sundberg, M. R. *Z. Anorg. Allg. Chem*. **2007**, *633*, 298.

(c) Barcelo-Oliver, M.; Garcia-Raso, A.; Terron, A.; Molins, E.; Prieto, M. J.; Moreno, V.; Martinez, J.; Llado, V.; Lopez, I.; Gutierrez, A.; Escriba, P. V. *J. Inorg. Biochem*. **2007**, *101*, 649.

(d) Baul, T. S. B.; Chaurasiya, A.; Duthie, A.; Montes-Tolentino, P.; Höpfl, H. *Cryst. Growth Des*. **2019**, *19*, 6656.

(e) Perez, S. J. L. P.; Atayde, E. C.; Arco, S. D. *J. Chin. Chem. Soc*. **2020**, *67*, 1.

6. (a) Devereux, M.; McCann, M.; Leon, V.; McKee, V.; Ball, R. J. *Polyhedron* **2002**, *21*, 1063.

(b) Ma, C. B.; Chen, C. N.; Liu, Q. T.; Liao, D. Z.; Li, L. C. *Eur. J. Inorg. Chem*. **2003**, 1227.

7. Xie, C. Z.; Yu, B.; Wang, X. Q.; Shen, R. J. W. G. Q.; Shen, D. Z. *J. Coord. Chem*. **2006**, *59*, 2005.

8. (a) Kim, S. H.; Park, B. K.; Song, Y. J.; Yu, S. M.; Koo, H. G.; Kim, E. Y.; Poong, J. I.; Lee, J. H.; Kim, C.; Kim, S. J.; Kim, Y. *Inorg. Chim. Acta* **2009**, *362*, 4119.

(b) Kwak, H.; Lee, S. H.; Kim, S. H.; Lee, Y. M.; Park, B. K.; Lee, Y. J.; Jun, J. Y.; Kim, C.; Kim, S. J.; Kim, Y. *Polyhedron* **2009**, *28*, 553.

(c) Humphrey, S. M.; Wood, P. T. *J. Am. Chem. Soc*. **2004**, *126*, 13236.

(d) Liu, Y. L.; Kravtsov, V. C.; Beauchamp, D. A.; Eubank, J. F.; Eddaoudi, M. *J. Am. Chem. Soc.* **2005**, *127*, 7266.

(e) Wei, Y. L.; Hou, H. W.; Li, L. K.; Fan, Y. T.; Zhou, Y. *Cryst. Growth Des*. **2005**, *15*, 1405.

9. Ay, B.; Yildiz, E.; Kani, I. *Polyherdron* **2017**, *130*, 165.

10. (a) Shahraki, S.; Shiri, F.; Majd, M. H.; Razmara, Z. *J. Pharmaceut. Biomed*. **2017**, *145*, 273.

(b) Altay, A.; Caglar, S.; Caglar, B.; Sahin, Z. S. *Inorg. Chim. Acta* **2019**, *493*, 61.

(c) Gangu, K. K.; Maddila, S.; Mukkamala, S. B.; Jonnalagadd, S. B. *Polyhedron* **2019**, *158*, 464.

11. (a) Cook, T. R.; Zheng, Y. R.; Stang, P. J. *Chem. Rev*. **2013**, *113*, 734.

(b) Lehn, J. M.; Atwood, J. L.; Davies, J. E. D.; MacNicol, D. D.; Vogtle F. (Eds.), Comprehensive Supramolecular Chemistry, Pergamon, Oxford, UK, **1996**.

12. Dutta, D.; Chetry, S.; Gogoi, A.; Choudhury, B.; Guha, A. K; Bhattacharyya, M. K. *Polyhedron* **2018**, *151*, 381.

13. Saha, U.; Dutta, D.; Nath, H.; Franconetti, A.; Frontera, A.; Bhattacharyya, M. K. *Inorg. Chim. Acta* **2019**, *488*, 159.

14. (a) Frontera, A.; Gamez, P.; Mascal, M.; Mooibroek, T. J.; Reedijk, J. *Angew. Chem. Int. Ed.* **2011**, *50*, 9564.

(b) Bauza, A.; Mooibroek, T. J.; Frontera, A. *Chem. Phys. Chem.* **2015**, *16*, 2496.

15. Estarellas, C.; Frontera, A.; Quinonero, D.; Deya, P. M. *Angew. Chem. Int. Ed*. **2011**, *50*, 415.

16. Mooibroek, T. S.; Teat, S. J.; Massera, C.; Reedijk, J. *Cryst. Growth Des*. **2006**, *6*, 1569.

17. Mooibroek, T. J.; Gamez, P.; Reedijk, J. *CrystEngComm.* **2008**, *10*, 1501.

18. Estarellas, C.; Frontera, A.; Quiñonero, D.; Deyà, P.M. *Cent. Eur. J. Chem*. **2011**, *9*, 25.

19. Głowacki, E. D.; Irimia-Vladu, M.; Bauer, S.; Sariciftci, N. S. *J. Mater. Chem.* **2013**, *B1*, 3742.

20. Maccallum, E. H.; Poet, R.; Milner-White, E. J. *J. Mol. Biol*. **1995**, *248*, 361.

21. Allen, F. H.; Baalham, C. A.; Lommerse, J. P. M.; Raithby, P. R. *Acta Cryst.* **1998**, *B54*, 320.

22. SADABS, V2.05, Bruker AXS, Madison, USA, **1999**.

23. Sheldrick, G. M. *Acta Crystallogr*. **2008**, *64*, 112.

24. Brandenburg, K. Diamond 3.1f, Crystal Impact GbR, Bonn, Germany, **2008**.

25. Frisch, M. J.; Trucks, G. W.; Schlegel, H. B.; Scuseria, G. E.; Robb, M. A.; Cheeseman, J. R.; Scalmani, G.; Barone, V.; Mennucci, B.; Petersson, G. A.; Nakatsuji, H.; Caricato, M.; Li, X.; Hratchian, H. P.; Izmaylov, A. F.; Bloino, J.; Zheng, G.; Sonnenberg, J. L.; Hada, M.; Ehara, M.; Toyota, K.; Fukuda, R.; Hasegawa, J.; Ishida, M.; Nakajima, T.; Honda, Y.; Kitao, O.; Nakai, H.; Vreven, T.; Montgomery Jr, J. A.; Peralta, J. E.; Ogliaro, F.; Bearpark, M.; Heyd, J. J.; Brothers, E.; Kudin, K. N.; Staroverov, V. N.; Kobayashi, R.; Normand, J.; Raghavachari, K.; Rendell, A.; Burant, J. C.; Iyengar, S. S.; Tomasi, J.; Cossi, M.; Rega, N.; Millam, J. M.; Klene, M.; Knox, J. E.; Cross, J. B.; Bakken, V.; Adamo, C.; Jaramillo, J.; Gomperts, R.; Stratmann, R. E.; Yazyev, O.; Austin, A. J.; Cammi, R.; Pomelli, C.; Ochterski, J. W.; Martin, R. L.; Morokuma, K.; Zakrzewski, V. G.; Voth, G. A.; Salvador, P.; Dannenberg, J. J.; Dapprich, S.; Daniels, A. D.; Farkas, O.; Foresman, J. B.; Ortiz, J. V.; Cioslowski, J.; Fox, D. J. *Gaussian 09, Gaussian, Inc.*, Wallingford C.T. **2009**.

26. Grimme, S.; Antony, J.; Ehrlich, S.; Krieg, H. *J. Chem. Phys*. **2010**, *132*, 154104.

27. Boys, S. F.; Bernardi, F. *Mol. Phys*. **1970**, *19*, 553.

28. Contreras-García, J.; Johnson, E. R.; Keinan, S.; Chaudret, R.; Piquemal, J. P.; Beratan, D. N.; Yang, W. *J. Chem. Theory Comput*. **2011**, *7*, 625.

29. (a) Mosmann, T. *J. Immunol. Methods* **1983**, *65*, 55.

(b) Verma, A. K.; Prasad, S. B. *Anticancer Agents Med. Chem*. **2013**, *13*, 1096.

30. Jones, G.; Wortberg, M.; Kreissig, S. B.; Bunch, D. S.; Gee, S. J.; Hammock, B. D.; Rocke, D. M. *J. Immunol. Methods* **1994**, *177*, 1.

31. (a) Squier, M. K.; Cohen, J. J. *Mol. Biotechnol*. **2001**, *19*, 305.

(b) Prasad, S. B.; Verma, A. K. *Microsc. Microanal*. **2013**, *19*, 1377.

32. Thomsen, R.; Christensen, M. H. *J. Med. Chem*. **2006**, *49*, 3315.

33. Pettersen, E. F.; Goddard, T. D.; Huang, C. C.; Couch, G. S.; Greenblatt, D. M.; Meng, E. C.; Ferrin, T. E. *J. Comput. Chem*. **2004**, *25(13)*, 1605.

34. Al-Sha'er, M. A.; Al-Balas, Q. A.; Hassan, M. A.; Al Jabal, G. A.; Almaaytah, A. M. *Comput. Biol. Chem*. **2019**, *80*, 102.

35. Wolber, G.; Langer, T. *J. Chem. Inf. Model* **2005**, *45*, 160.

36. Nath, H.; Sharma, P.; Frontera, A.; Verma, A. K.; Das, A.; Barceló-Oliver, M.; Bhattacharyya, M. K. *Polyhedron* **2020**, *176*, 114266.

37. Sjöström. M.; Kolman, A.; Clemedson, C.; Clothierc, R. *Toxicol. In Vitro* **2009**, *22*, 1405.

38. (a) Banerjee, A.; Chattopadhyay, S. *Polyhedron* **2020**, *177*, 114290.

(b) Hamil, A.; Khalifa, K. M.; Almutaleb, A. A.; Qasim, M.; *Adv. J. Chem*. **2020**, *3*, 524.

39. (a) Bellamy, L. J. The Infrared Spectra of Complex Molecules, second ed., **1980** *vol. 2*, Chapman & Hall, London/New York.

(b) Nakamoto, K. Infrared and Raman Spectra of Inorganic and Coordination Compound, fifth ed., Wiley, New York, **1997**.

40. Orhan, O.; Çolak, A. T.; Emen, F. M.; Kismali, G.; Meral, O.; Sel, T.; Çilgi, G. K.; Taş, M. *J. Coord. Chem*. **2015**, *68*, 4003.

41. (a) Ay, B.; Yildiz, E.; Kani, I. *J. Solid State Chem*. **2016**, *233*, 44.

(b) Yang, L.; Liu, L.; Wu, L.; Zhang, H.; Song, S. *Dyes Pigment*. **2014**, *105*, 180.

(c) Łyszczek, R.; Mazur, L. *Polyhedron* **2012**, *41*, 7.

42. Vargova, Z.; Zeleoak, V.; Cisaoova, I.; Gyoryova, K. *Thermochim. Acta* **2004**, *423*, 149.

43. Yang, R.; Li, H. H.; Hecke, K. V.; Cui, G. H. *Bioinorg. Chem. Appl*. **2015**, *641*, 642.

44. Dogan, D.; Colak, A. T.; Sahin, O.; Tunc, T.; Celik, O. *Polyhedron* **2015**, *93*, 37.

45. Hojnik, N.; Kristl, M.; Ferk, G.; Golobič, A.; Turel, M.; Jagličić, Z.; Drofenik, M. *J. Coord. Chem.* **2016**, *69*, 1484.

46. Bora, S. J.; Das, B. K. *J. Solid State Chem*. **2012**, *192*, 93.

47. Dogan, D.; Colak, A. T.; Sahin, O.; Tunc, T.; Celik, O. *Polyhedron* **2015**, *93*, 37.

48. Soares-Santos, P. C. R.; Cunha-Silva, L.; Almeida Paz, F. A.; Sa´ Ferreira, R. A.; Rocha, J.; Trindade, T.; Carlos, L. D.; Nogueira, H. I. S. *Cryst. Growth Des*. **2008**, *8*, 2505.

49. (a) Srinivasan, S.; Annaraj, J.; Athappan, P. R. *J. Inorg. Biochem*. **2005**, *99*, 876.

(b) Bruijnincx, P. C. A.; Sadler, P. J. *Curr. Opin. Chem. Biol*. **2008**, *12*, 197.

50. Ghosh, M.; Majee, A.; Nethaji, M.; Chattopadhyay, T. *Inorg. Chim. Acta* **2009**, *362*, 2052.

51. Gogoi, A.; Islam, S. M. N.; Frontera, A.; Bhattacharyya, M. K. *Inorg. Chim. Acta* **2019**, *484*, 133.

52. (a) Wang, D.; Tian, Z.; Wang, F.; Wen, L.; Li, D. *J. Inorg. Organomet. Polym*. **2009**, *19*, 196.

(b) Dogan, D.; Colak, A. T.; Sahin, O.; Tunc, T.; Celik, O. *Polyhedron* **2015**, *93*, 37.

(c) Kumagai, H.; Sobukawa, H.; Kurmoo, M. *J. Mater. Sci.* **2008**, *48*, 2123.

53. (a) Das, A; Choudhury, S. R.; Estarellas, C.; Dey, B.; Frontera, A.; Hemming, J.; Helliwell, M.; Gamez, P.; Mukhopadhyay, S. *CrystEngComm.* **2011**, *13*, 4519.

(b) Islam, S. M. N.; Dutta, D.; Sharma, P.; Verma, A. K.; Frontera, A.; Bhattacharyya, M. K. *Inorg. Chim. Acta* **2019**, *498*, 119108.

54. Manna, P.; Seth, S. K.; Das, A.; Hemming, J.; Prendergast, R.; Helliwell, M.; Choudhury, S. R.; Frontera, A.; Mukhopadhyay S. *Inorg. Chem.* **2012**, *51*, 3557.

55. Mitra, M.; Manna, P.; Bauza, A.; Ballester, P.; Seth, S. K.; Choudhury, S. R.; Frontera, A.; Mukhopadhyay, S. *J. Phys. Chem.* **2014**, *B118*, 14713.

56. Etter, M. C. *Acc. Chem. Res*. **1990**, *23*, 120.

57. (a) Gogoi, A.; Dutta, D.; Verma, A. K.; Nath, H.; Frontera, A.; Guha, A. K.; Bhattacharyya, M. K. *Polyhedron* **2019**, *168*, 113.

(b) Gogoi, A., Das, A., Frontera, A; Verma, A. K.; Bhattacharyya, M. K. *Inorg. Chim. Acta* **2019**, *493*, 1.

58. Fábián, L.; Kálmán, A., *Acta Cryst*. **1999**, *B55*, 1099.

59. Croitor, L.; Chisca, D.; Coropceanu, E. B.; Volodina, G. F.; Petuhov, O.; Fonari, M. S. *J. Mol. Struct*. **2017**, *1137*, 136.

60. Borah, S.; Kalita, A. C.; Gogoi, N. *Z. Anorg. Allg. Chem*. **2014**, *640*, 1789.

61. Balić, T.; Popović, Z.; Marković, B. *Inorg. Chim. Acta* **2018**, *478*, 32.

62. (a) Vener, M. V.; Egorova, A. N.; Churakov, A. V.; Tsirelson, V. G. *J. Comput. Chem.* **2012**, *33*, 2303.

(b) Choudhary, A.; Kamer, K. J.; Raines, R. T. *J. Org. Chem*. **2011**, *76*, 7933.

63. Vener, M. V.; Egorova, A. N.; Churakov, A. V.; Tsirelson, V. G. *J. Comput. Chem*. **2012**, *33*, 2303.

64. Jin, J.; Han, X.; Meng, Q.; Li, D.; Chi, Y.; Niu, S. *J. Solid State Chem*. **2013**, *197*, 92.

65. Yesilel, O. Z.; Olmez H. *J. Therm. Anal. Cal*. **2006**, *86*, 211.

66. Gangu, K. K.; Mukkamala, S.B. Synthesis *and Reactivity in Inorganic, Metal-Organic, and Nano-Metal Chemistry* **2016**, *46*, 98.

67. Devereux, M.; McCann, M.; Cronin, J. F.; Cardin, C.; Todd, A.; *Polyhedron* **1996**, *15*, 785.

68. Kumar, S.; Bajaj, S.; Bodla, R. B. *Indian J. Pharmacol*. **2016**, *48*, 481.

69. Sebaugh, J. L. *Pharm. Stat.* **2011**, *10*, 128.

70. Curcic, M. G.; Stankovic, M. S.; Mrkalic, E. M.; Matovic, Z. D.; Bankovic, D. D.; Cvetkovic, D. M.; Dacic, D. S.; Markovic, S. D. *Int. J. Mol. Sci.* **2012**, *13*, 2521.

71. Oh, H.; Livingston, R.; Smith, K.; Garcia, L. A. *MURJ* **2004**, *11*, 53.

72. Sathishkumar, N.; Sathiyamoorthy, S.; Ramya, M.; Yang, D. U.; Lee, H. N.; Yang, D. C. *J. Enzyme Inhib. Med. Chem*. **2012**, *27*, 685.

73. Certo, M.; Moore, V. D. G.; Nishino, M.; Wei, G.; Korsmeyer, S.; Armstrong, S. A.; Letai A. *Cancer cell* **2006**, *9*, 351.

74. (a) Garcia-Saez, A. *Cell Death Differ*. **2012**, *19*, 1733.

(b) Wei, M. C.; Zong, W.-X.; Cheng, E. H. Y.; Lindsten, T.; Panoutsakopoulou, V.; Ross, A. J.; Roth, K. A.; MacGregor, G. R.; Thompson, C. B.; Korsmeyer, S. J. *Science* **2001**, *292*, 727.

75. Frenzel, A.; Grespi, F.; Chmelewskij, W.; Villunger, A. *Apoptosis* **2009**, *14(4)*, 584.

76. Soderquist, S.; Alan, E. *Mol.* Cancer *Ther.* **2016**, *15*, 2011.

77. Wolber, G.; Langer, T. *J. Chem. Inf. Model* **2005**, *45*, 160.